9

Planar lightwave circuits in fiber-optic communications

Christopher R. Doerr[*] and Katsunari Okamoto[†]

[*]*Alcatel-Lucent, Holmdel, NJ, USA*
[†]*Okamoto Laboratory, Mito-shi, Ibaraki-ken, Japan*

9.1 INTRODUCTION

Non-technical overview: Planar lightwave circuits are optical "chips" that are usually connected to optical fibers and perform various functions such as wavelength filtering, optical switching, and optical channel power control. They are used mostly in fiber-optic communication networks. They are sometimes also called "photonic integrated circuits," "integrated optics," "optical benches," or "waveguides." They can be made of several different materials, the most common being glass waveguides on top of a silicon wafer or InGaAsP waveguides on an InP wafer.

Planar lightwave circuits (PLCs) are a planar arrangement of waveguides on a substrate. PLCs exist in many different material systems, including SiO_2, SiON, polymer, Si, GaAs, InP, and $LiNbO_3$. In this chapter, we mainly focus on the lower refractive index materials, SiO_2, SiON, and polymer, mainly because we can cover only so much in one chapter, and also because another chapter in this volume covers InP PLCs.

Compared to electronic integrated circuits (EICs), photonic integrated circuits (PICs) (another name for PLCs) are simple. Whereas EICs commonly integrate millions of components, today's PICs integrate at most hundreds of components. In fact, the PIC market is still mainly dominated by simple optical couplers/splitters for fiber-to-the-home applications. One of the main reasons is that it is easier to achieve a strong nonlinear response with electrons than with photons. Another reason is that the wavelength of an electron is much smaller than the wavelength of a photon, facilitating much more dense integration of EICs than PICs.

However, whereas electrons win over photons in the particle picture, in the wave picture optics win over electronics. In the wave picture, optics and electronics are not so different, optics simply being electromagnetic waves oscillating at

Optical Fiber Telecommunications V A: Components and Subsystems

ISBN: 978-0-12-374171-4

terahertz frequencies and higher, whereas electronics are usually considered as electromagnetic waves oscillating at gigahertz frequencies and lower. Using optics as a carrier, extremely high signal bandwidths can be transported. The optical fiber provides a low-loss medium to do this, and optical amplifiers can re-amplify the signal with nearly ideal noise levels.

This chapter focuses on PLCs used with signal-transporting optical fibers. There are two main ways to achieve high bandwidth on an optical fiber, and PLCs are instrumental in both. One is to increase the number of "channels" on a fiber, each channel being at a different carrier frequency (or equivalently wavelength). This is called wavelength-division multiplexing (WDM), and inter-channel control PLCs play a large role here, serving mainly as channel multiplexers and demultiplexers. The other method to increase bandwidth is to increase the signal rate itself, and intra-channel control PLCs are beginning to play a significant role here, as well, serving, for example, as optical dispersion compensators and general optical equalizers.

9.2 BASIC WAVEGUIDE THEORY AND MATERIALS

9.2.1 Index Contrast

Probably the most important parameter in PLCs is the refractive index difference between the core and the cladding, often referred to as "delta":

$$\Delta = \frac{n_{\text{core}}^2 - n_{\text{cladding}}^2}{2n_{\text{core}}^2} \approx \frac{n_{\text{core}} - n_{\text{cladding}}}{n_{\text{core}}} \tag{9.1}$$

For silica (SiO_2) PLCs with buried waveguides, a typical $\Delta = 0.008$, usually called "0.8%" and can be as high as 0.015 [1]. For SiON PLCs with buried waveguides, Δ can be significantly higher, as much as 0.14 [2]. For semiconductor PLCs, such as InP and Si, Δ can range from typically 0.01 for buried waveguides to as high as 0.45 for air-clad waveguides. The largest possible value of Δ is 0.5.

Δ determines how many modes a certain waveguide size will guide, how tight a curve can be, and how much coupling there will be between neighboring waveguides. A useful number derived from Δ is the V-number. For slab waveguides,

$$V = \frac{\pi n_{\text{core}} w}{\lambda_0}\sqrt{2\Delta}, \tag{9.2}$$

where w is the waveguide width and λ_0 is the free-space wavelength. If the waveguide has a finite height, then Δ should be an effective Δ, found using the effective index method. The number of modes guided by the waveguide is $2V/\pi$.

It is commonly accepted that if $\Delta < 0.007$, it is "low delta," if $0.007 < \Delta < 0.009$, it is "medium delta," and if $\Delta > 0.009$ it is "high delta."

9.2.2 Optical Couplers/Splitters

Non-technical overview: An optical splitter splits an optical signal on one waveguide into multiple copies of the signal on different waveguides. An optical coupler (also called a combiner) is an optical splitter operated in reverse.

All couplers are actually $N \times N$ couplers, where N is an integer, because of the conservation of the number of modes in a closed, static system. However, some of the input or output modes might be radiation modes (which must be treated carefully, because radiation modes are a continuum). For example, a 1×2 coupler is really a 2×2 coupler with one "port" being a radiation mode. Also, in optics, most couplers are directional couplers, in that there are distinct inputs and distinct outputs. For example, if light enters one port of a 2×2 optical coupler, it exits at most only two ports of the coupler. However, historically, the term "directional coupler" has been reserved for evanescent couplers only.

Coupler action can be divided into two main categories: power splitting or mode separation (sometimes called mode evolution) [3] (or equivalently, power combining and mode combining). Of course, all couplers are really power splitters (or combiners), but in this terminology, power splitting means that energy that started in one local normal mode of the coupler at the coupler input is distributed among a plurality of local normal modes at some point in the coupler. A good example is the multimode interference (MMI) coupler. In contrast, mode separation means that energy that started in one local normal mode of the coupler at the coupler input always stays in one local normal mode. It originates from the concept of demultiplexing multiple modes in a single wide waveguide into multiple narrow waveguides, one mode in each. A good example is the adiabatic directional coupler.

However, we do not recommend to be strict about this categorization. This is because when waveguides are far apart, it is ambiguous whether the local normal mode is the mode in each individual waveguide or the mode of the entire structure. For example, for two narrow waveguides that are far apart, there are two choices for the set of two local normal modes. One is that the local normal modes are the mode of each individual waveguide; the other is that the local normal modes are the even and odd modes of the two waveguides viewed as a larger structure. Another reason is that, as pointed out in Ref. [4], practical mode-separation couplers are not truly adiabatic in the same sense of the definition as is used in other branches of physics, such as thermodynamics or quantum mechanics. This is because the phase slip between modes in an adiabatic coupler is usually not many π, otherwise the coupler would be far too long.

1×2 Couplers

The two most popular optical 1×2 couplers are the Y-branch coupler and the 1×2 MMI coupler, shown in Figures 9.1 and 9.2. The Y-branch is best for use in low Δ materials, and the MMI is best for use in high Δ materials. This is because the Y-branch requires a very narrow gap, whereas an MMI has much wider gaps.

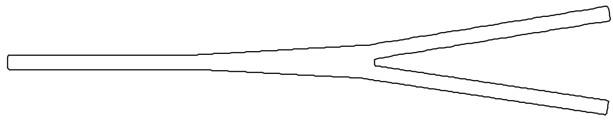

Figure 9.1 Y-Branch coupler.

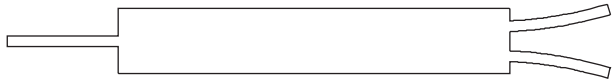

Figure 9.2 1×2 MMI coupler.

Also, the principle of operation for an MMI coupler requires high Δ. However, the MMI waveguide width must be accurate to avoid excess insertion loss. Both have a robust coupling magnitude and phase, the magnitude squared being 50/50 and the relative phase being 0°. This is because of the symmetry in their layouts.

A 1×2 coupler is actually a 2×2 coupler with one input/output being a radiation mode. For example, if two signals enter the Y-branch coupler from the right side and they are out of phase, then the combined energy radiates away on both sides of the single waveguide, none of the energy ending up in the waveguide.

2×2 Couplers

There are many choices for 2×2 couplers. A 2×2 coupler is much more challenging to make than a 1×2 coupler because there is no longer symmetry about the input waveguide. In other words, because the two output waveguides are placed symmetrically about the input waveguide in a 1×2 coupler, the splitting magnitude squared is always 50/50, and the splitting phase is always 0. In a 2×2 coupler, it must be designed just right to get a 50/50 splitting magnitude squared and/or a desired splitting phase. Wavelength, polarization, and fabrication (WPF) changes can call affect the splitting characteristics. The action of a 2×2 coupler is conveniently written as a rotation matrix R(θ). θ is $\pi/4$ for a 50/50 coupler.

2×2 couplers are useful for switches and, as we will see later, for making optical filters with flat-top passbands with low insertion loss.

One type is the "directional coupler," shown in Figure 9.3, also called the evanescent coupler. It consists of two waveguides brought close enough together to couple. It has the lowest insertion loss of any 2×2 coupler. If the directional coupler is symmetric about a horizontal line, then the splitting phase is always

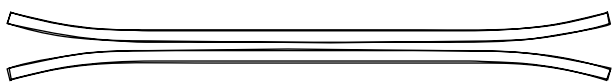

Figure 9.3 Directional coupler.

Figure 9.4 2×2 MMI coupler.

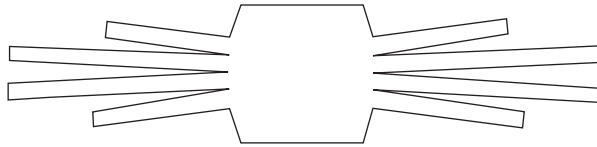

Figure 9.5 2×2 star coupler.

precisely 90°. The splitting magnitude varies with the length of the coupler. The length must be chosen just right to get a 50/50 splitting magnitude squared ratio, making the directional coupler highly sensitive to WPF changes.

Another type is the 2×2 MMI coupler (Figure 9.4). The MMI coupler is basically the same as the directional coupler with the gap filled in. Whereas the directional coupler is best used in low Δ waveguides, the MMI coupler is best used in high Δ waveguides. Whereas the directional coupler theoretically has zero excess loss, the MMI coupler has some intrinsic excess loss. The MMI coupler is less sensitive than the directional coupler to WPF changes, but it is still quite sensitive.

Another choice is the 2×2 star coupler (Figure 9.5). The star coupler is well known from its use in the arrayed waveguide grating (AWG). The star coupler is relatively robust to WPF changes. However, whereas an $N \times N$ star coupler, where N is large, can have very low loss, a 2×2 star coupler has high excess loss, typically at least 1 dB. This is because the waveguides converge and diverge too rapidly for a reasonable adiabatic transition. Nevertheless, the 2×2 star coupler is extremely valuable for avoiding polarization crosstalk and other fabrication sensitivities because each waveguide always sees a symmetric environment, unlike all the other 2×2 couplers discussed in this section, and is one of the reasons why the AWG is so successful.

The rest of the choices are all variations of the directional coupler, designed so as to mitigate the splitting magnitude ratio sensitivity to WPF changes. There exists a basic uncertainty principle in that as the coupler is desensitized in splitting magnitude, it is sensitized to splitting phase.

The first such coupler we describe is the asymmetric directional coupler. This is simply a directional coupler with one waveguide much wider than the other. In a symmetric directional coupler, as the coupler length increases the splitting magnitude squared goes all the way from 0/100 to 100/0. In an asymmetric directional coupler (Figure 9.6), the coupling never reaches 100/0 because the propagation speed in the two waveguides is different. The coupler is designed such that the maximum power transfer reaches at most 50% before the coupled light becomes out of phase with the incoming coupled light. Thus, the splitting magnitude is

Figure 9.6 Asymmetric directional coupler.

Figure 9.7 Adiabatic directional coupler.

insensitive to wave length changes to first order. However, the splitting ratio is highly sensitive to changes in the waveguide width, and thus, the asymmetric directional coupler is rarely used in practical devices.

An elegant 2×2 coupler is the adiabatic directional coupler (Figure 9.7). This directional coupler simply starts with two waveguides of different widths and transitions gradually to two waveguides of the same width. If the transition is slow enough to not exchange energy between local normal modes, i.e., adiabatic, then the splitting magnitude squared ratio is precisely 50/50. This is because the mode in the wider waveguide on the left becomes the symmetric mode of the two waveguides on the right, and the mode in the narrow waveguide on the left becomes the anti-symmetric mode on the right. The two drawbacks to this coupler are that it is very long and that the splitting phase is highly uncertain in the right-to-left propagation direction (precisely 0 in the left-to-right propagation direction).

Probably the most practical WPF-desensitized directional coupler is the multi-section directional coupler. Designs with two [5], three [6], and four [7] sections have been demonstrated. Figure 9.8 shows a two-section example. One example is a two-section coupler with the first and second sections having a nominal 50/50 and 100/0 splitting magnitude squared ratios, respectively, with a relative path-length difference of 120° between the two sections. For a three-section coupler, a good 50/50 design is to make all three sections have the same length and nominal 50/50, and have 0° phase between the first and the second section and 120° phase between the second and the third sections.

The final WPF-desensitized directional coupler we discuss is the curved directional coupler (Figure 9.9) [8]. This operates on the same principle as the asymmetric directional coupler in that the bending results in the coupled light becoming out of phase before full coupling occurs. A significant advantage over the asymmetric coupler is that both waveguides have the same width, and thus, it is not sensitive to waveguide width

Figure 9.8 Multi-section directional coupler.

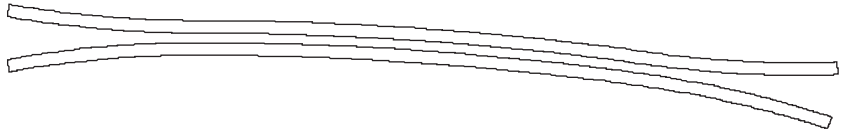

Figure 9.9 Curved directional coupler.

changes like the asymmetric directional coupler is. This coupler is the most compact WPF-desensitized directional coupler. Unfortunately, this coupler appears to exhibit significant polarization crosstalk when implemented in silica waveguides, and research is ongoing to mitigate this.

9.2.3 Polarization Effects

Non-technical overview: The oscillating electric field that makes up the optical signal can be oscillating predominantly either parallel to the PLC surface or perpendicular to it and in the direction of propagation. Which direction the electric field is oscillating determines its polarization. The light in PLCs usually travels faster or slower depending on its polarization due to birefringence. Birefringence can result from the molecular structure of the material in the waveguide, strain in the waveguide, or the waveguide shape.

Because PLCs are planar, they tend to have birefringence. Birefringence means that there are two different refractive indices for the two optical polarizations in the chip. The two polarizations are commonly called transverse electric (TE) and transverse magnetic (TM) polarizations, where TE has an electric field component parallel to the surface of the PLC, and TM has a magnetic field component parallel to the surface of the PLC. Note that eigenmodes of PLC waveguides are only truly TE and TM for slab waveguides. Modes of waveguides with side walls, i.e., most real PLC waveguides, cannot be perfect TE or TM modes and should be called quasi-TE and quasi-TM modes.

Birefringence results in a polarization-dependent wavelength (PDW) shift in PLC optical filters. It is important to realize that PDW shift is a function only of the birefringence. No matter what the channel spacing, bandwidth, etc. of a filter, it will always have the same PDW shift in a given birefringent PLC material.

The main sources of the birefringence are strain and geometry. In silica PLCs, the dominant source of birefringence is strain, whereas in InP PLCs, the dominant source of birefringence is geometry. Suppose we consider an optical filter that has a passband. If we define PDW = passband peak wavelength for TM − passband peak wavelength for TE, then silica typically has a PDW = + 0.05 nm, and InP typically has a PDW = −3.0 nm.

The most common way to eliminate PDW in silica is to reduce the strain on the cores by doping the upper cladding glass so that its expansion coefficient matches that of the silicon substrate. The most common way to eliminate PDW in InP is to

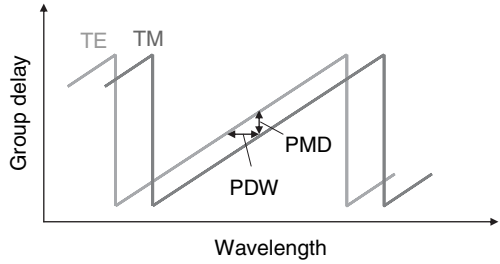

Figure 9.10 Group delay vs wavelength for a typical dispersion compensator, showing how PDW shift results in PMD (this figure may be seen in color on the included CD-ROM).

choose just the right waveguide height and width and layer composition. As the index contrast between core and cladding increases, it can become nearly impossible to achieve a low PDW because of the fabrication sensitivities. In such a case, other schemes, such as polarization diversity where two copies of the filter are made, one to handle each polarization, are employed.

If the optical filter has a nonlinear phase response, such as a dispersion compensator does, then PDW shift results in polarization-mode dispersion (PMD), as shown in Figure 9.10. PMD $= |\text{PDW} \times \text{CD}|$, where CD is the chromatic dispersion.

Another effect that must be considered in PLCs is polarization crosstalk, also called polarization conversion. One might expect that because PLCs are planar, if a signal is launched as TE or TM into one end of the chip, it will exit in the same polarization. This is often untrue. If the signal ever experiences a condition where the local axis of strain or geometrical symmetry is not parallel or perpendicular to the PLC surface, polarization crosstalk can occur. Polarization crosstalk is especially prevalent in directional couplers [9] but can also be seen in bends [10] and even at the sidewalls of straight high-index-contrast straight waveguides [11].

Polarization crosstalk is problematic when trying to achieve polarization-insensitive destructive interference in an interferometer, such as is needed in variable optical attenuators (VOAs) and Mach–Zehnder delay interferometers (MZDIs) (see Figure 9.11). The PDW shift of an MZDI must typically be smaller than what can be achieved due to open-loop process birefringence control (for silica, 50 pm is possible, but <4 pm is often required). Thus, in the design of Figure 9.11, there is a thin half-wave plate inserted half-way through the MZDI. The waveplate swaps TE and TM half-way through the interferometer, thus achieving a net zero PDW shift for the interferometer, regardless of the waveguide birefringence. However, polarization crosstalk in the directional couplers prevents the half-wave plate from achieving a perfect zero net PDW shift. To minimize the polarization crosstalk, the design of Figure 9.11 uses "clamping," which consists of placing dummy waveguides around all the directional couplers in an effort to symmetrize the stress on the waveguides in the coupler.

However, the clamping solution can only partially equalize the stress on the upper and lower parts of the core. If the upper cladding is so heavily doped so as to make the

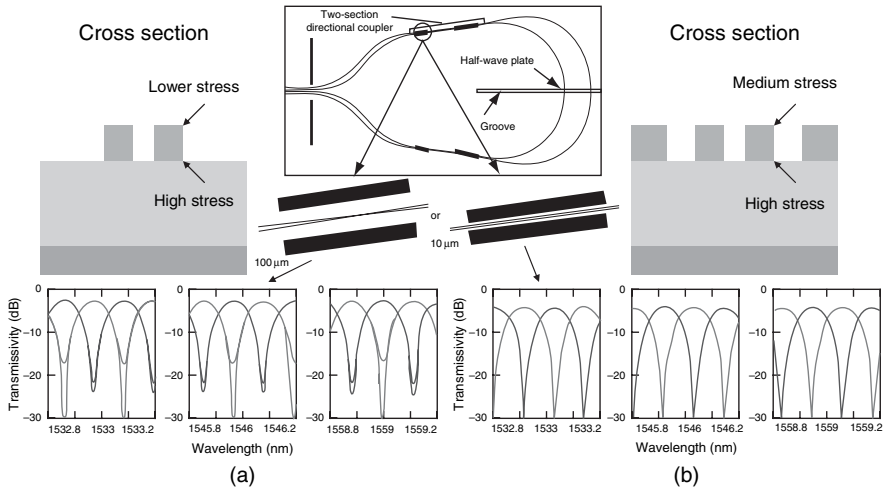

Figure 9.11 Mach–Zehnder delay interferometer made of multi-section directional couplers with coupler "clamping" to symmetrize stress on the coupled waveguides in order to mitigate polarization crosstalk (this figure may be seen in color on the included CD-ROM).

PDW shift zero or even negative (over compensation), we have found experimentally that significant polarization crosstalk in directional couplers occurs despite clamping.

A more robust approach is to use 2×2 star couplers instead of directional couplers (see Figure 9.5). This results in a perfectly symmetric environment for each waveguide, thus eliminating the polarization crosstalk. A Mach–Zehnder delay interferometer that uses star couplers to achieve low polarization crosstalk is described in Ref. [12]. The drawback is increased insertion loss due to the inefficiency of a 2×2 star coupler, and if the star coupler is not carefully designed, the phase difference between the two outputs when launching into one input of the star coupler will not be exactly 90°. The low polarization crosstalk of the star coupler is related to why AWGs usually do not exhibt polarization conversion—all the elements in a typical AWG provide a symmetric environment for all waveguides.

9.3 PASSIVE OPTICAL FILTERING, DEMODULATING, AND DEMULTIPLEXING DEVICES

This section covers passive devices that can filter and/or route wavelengths.

9.3.1 Mach–Zehnder Interferometers

A Mach–Zehnder interferometer (MZI) is an interferometer with two couplers and two arms. If one arm is longer than the other, then the MZI acts as an optical filter or optical demodulator.

Demodulators

Non-technical overview: A phase-shift keyed (PSK) signal has data encoded in the phase of the signal. Because a photodetector detects only optical power, the PSK signal must be converted to an amplitude-shift keyed (ASK) signal at the receiver. This can be done by interfering the signal with one or more delayed copies of itself or with a separate optical signal (i.e., a local oscillator).

Optical demodulators serve to convert PSK data to ASK data. The simplest example is a 1-bit delay, used to demodulate differential PSK (DPSK). It consists of an MZI with one arm longer by one bit length than the other; an example was shown in Figure 9.11.

A more complicated example is a differential quadrature PSK (DQPSK) demodulator. DQPSK consists of four phase levels. It can be demodulated using either two MZIs or one MZI with a 90° hybrid as the second coupler, as shown in Figure 9.12. A silica PLC implementation of the latter option, using a star coupler as the 90° hybrid, is shown in Figure 9.13.

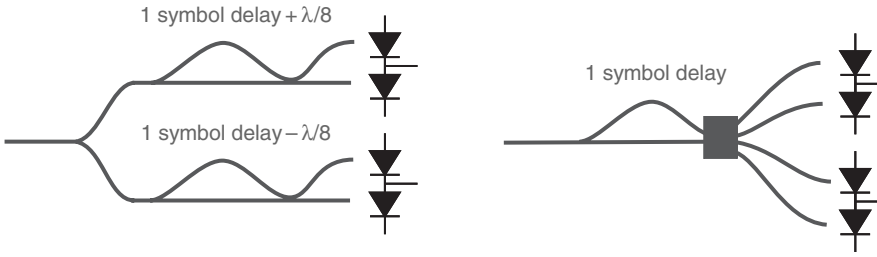

Figure 9.12 Two choices for a DQPSK demodulator (this figure may be seen in color on the included CD-ROM).

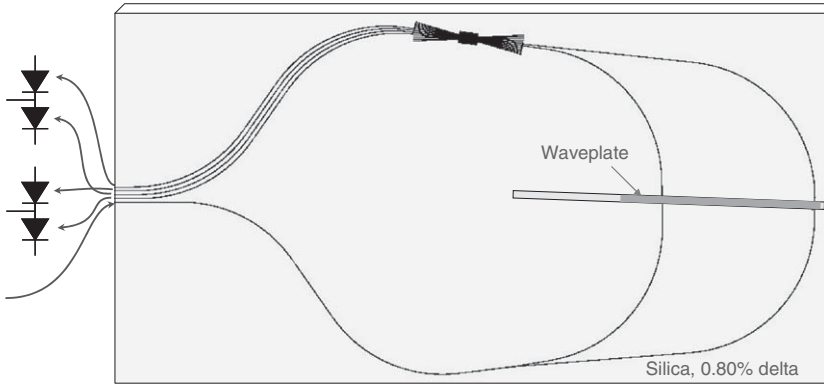

Figure 9.13 Silica PLC implementation of a DQPSK demodulator (this figure may be seen in color on the included CD-ROM).

Interleavers

Interleavers are 1×2 or 2×2 filters that are spectrally periodic. They can be made of concatenated MZIs and are discussed later on in this chapter.

9.3.2 Arrayed Waveguide Gratings

Non-technical overview: An AWG is somewhat analogous to a prism, in that it takes an input white light beam and separates it into many colored output light beams. This feature is called "demultiplexing" and is useful to separate out the signal channels at different wavelengths in an optical fiber. The device can also work in reverse, i.e., multiplex different colored light beams into one beam and is called "multiplexing." However, the prism analogy is imperfect, and AWGs can do much more, such as provide $N \times N$ wavelength routing and "colorless" routing.

The arrayed waveguide grating (AWG) is a generalized MZI. Other names for AWGs are PHASARs (phased arrays) and waveguide grating routers (WGRs). The basic AWG is shown in Figure 9.14. It consists of two $N \times N$ star couplers connected by an array of waveguides of linearly increasing path length.

An $N \times N$ AWG multiplexer is very attractive in optical WDM networks since it is capable of increasing the aggregate transmission capacity of a single strand optical fiber in a compact device that is relatively simple to manufacture [13–15]. The AWG consists of input/output waveguides, two focusing slab regions, and a phased array of multiple channel waveguides with a constant path-length difference ΔL between neighboring waveguides (Figure 9.14). In the first slab region, the input waveguide separation is D_1, the array waveguide separation is d_1, and the radius of curvature is f_1.

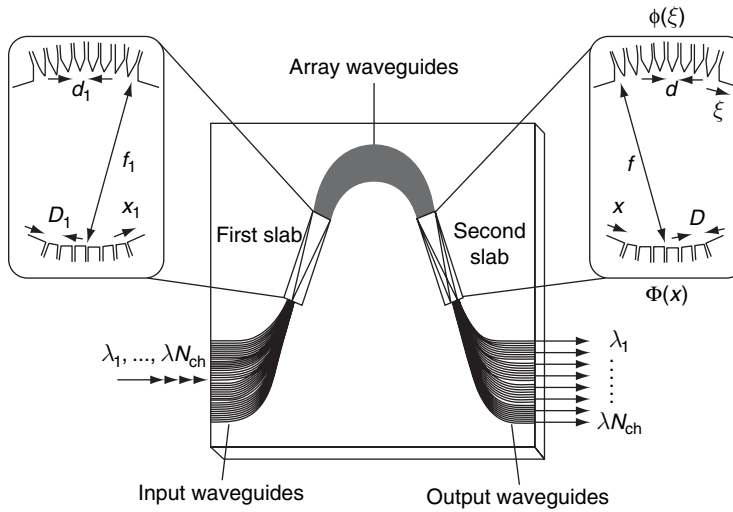

Figure 9.14 Schematic configuration of arrayed waveguide grating multiplexer.

Generally, the waveguide parameters in the first and the second slab regions may be different. Therefore, in the second slab region the output waveguide separation is D, the array waveguide separation is d, and the radius of curvature is f, respectively. The input light at the position of x_1 (x_1 is measured in a counter-clockwise direction from the center of input waveguides) is radiated to the first slab and then excites the arrayed waveguides. The excited electric field amplitude in each array waveguide is $a_i (i = 1 - N)$ where N is the total number of array waveguides. The amplitude profile a_i is usually a Gaussian distribution. After traveling through the arrayed waveguides, the light beams constructively interfere into one focal point x (x is measured in a counterclockwise direction from the center of the output waveguides) in the second slab. The location of this focal point depends on the signal wavelength because the relative phase delay in each waveguide is given by $2\pi\Delta L/\lambda$. Figure 9.15 shows an

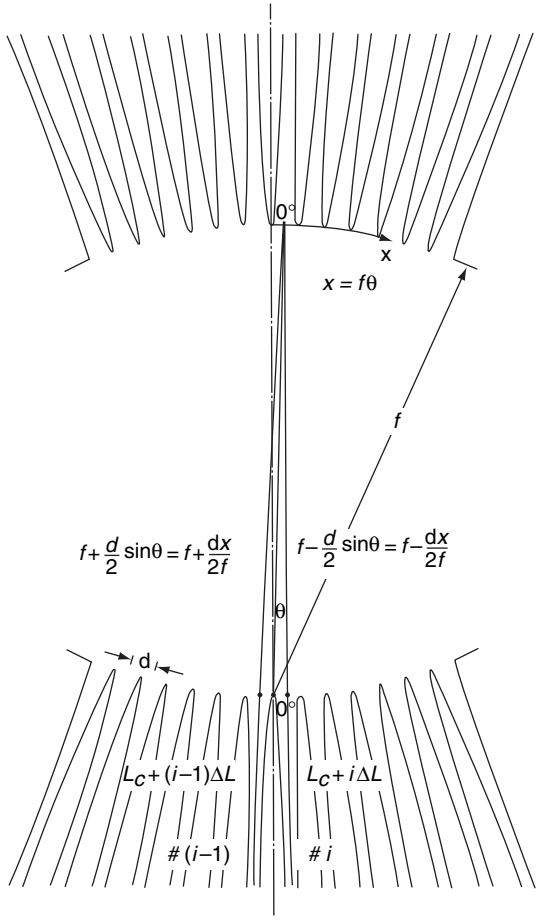

Figure 9.15 Enlarged view of the second slab region (rotated 180° from Figure 9.14).

enlarged view of the second slab region. Let us consider the phase retardations for the two light beams passing through the $(i-1)$-th and i-th array waveguides. The geometrical distances of two beams in the second slab region are approximated as shown in Figure 9.15. We have similar configurations in the first slab region as those in Figure 9.15. The difference of the total phase retardations for the two light beams passing through the $(i-1)$-th and i-th array waveguides must be an integer multiple of 2π in order that two beams constructively interfere at the focal point x. Therefore, we have the interference condition expressed by

$$\beta_s(\lambda_0)\left(f_1-\frac{d_1 x_1}{2f_1}\right)+\beta_c(\lambda_0)[L_c+(i-1)\Delta L]+\beta_s(\lambda_0)\left(f+\frac{dx}{2f}\right)$$
$$=\beta_s(\lambda_0)\left(f_1+\frac{d_1 x_1}{2f_1}\right)+\beta_c(\lambda_0)[L_c+i\Delta L]+\beta_s(\lambda_0)\left(f-\frac{dx}{2f}\right)-2m\pi, \tag{9.3}$$

where β_s and β_c denote the propagation constants in slab region and array waveguide, m is an integer, λ_0 is the center wavelength of WDM system, and L_c is the minimum array waveguide length. Subtracting common terms from Eqn (9.3), we obtain

$$\beta_s(\lambda_0)\frac{d_1 x_1}{f_1}-\beta_s(\lambda_0)\frac{dx}{f}+\beta_c(\lambda_0)\Delta L=2m\pi. \tag{9.4}$$

When the condition $\beta_c(\lambda_0)\Delta L=2m\pi$ or

$$\lambda_0=\frac{n_c\,\Delta L}{m} \tag{9.5}$$

is satisfied for λ_0, the light input position x_1 and the output position x should satisfy the condition

$$\frac{d_1 x_1}{f_1}=\frac{dx}{f}. \tag{9.6}$$

In Eqn (9.5), n_c is the effective phase index of the array waveguide ($2\pi n_c=\beta_c/k$, k: wavenumber in vacuum) and m is called the diffraction order. The above equation means that when light is coupled into the input position x_1, the output position x is determined by Eqn (9.6). Usually, the waveguide parameters in the first and the second slab regions are the same ($d_1=d$ and $f_1=f$). Therefore, input and output distances are equal as $x_1=x$. The spatial dispersion of the focal position x with respect to the wavelength λ for the fixed light input position x_1 is given by differentiating Eqn (9.4) with respect to λ as

$$\frac{\Delta x}{\Delta\lambda}\approx-\frac{N_c\,f\,\Delta L}{n_s\,d\,\lambda_0}, \tag{9.7}$$

where n_s is the effective index in the slab region, and N_c is the effective *group* index of the effective index n_c of the array waveguide ($N_c=n_c-\lambda dn_c/d\lambda$). The spatial

dispersion of the input-side position x_1 with respect to the wavelength λ for the fixed light output position x is given by

$$\frac{\Delta x_1}{\Delta \lambda} \approx \frac{N_c f_1 \Delta L}{n_s d_1 \lambda_0}. \tag{9.8}$$

The input and output waveguide separations are $|\Delta x_1| = D_1$ and $|\Delta x| = D$, respectively, when $\Delta\lambda$ is the channel spacing of the WDM signal. Putting these relations into Eqns (9.5) and (9.6), the wavelength spacing on the output side for a fixed light input position x_1 is given by

$$\Delta\lambda_{out} = \frac{n_s\, dD\lambda_0}{N_c\, f\Delta L}, \tag{9.9}$$

and the wavelength spacing on the input side for a fixed light output position x is given by

$$\Delta\lambda_{in} = \frac{n_s\, d_1 D_1 \lambda_0}{N_c f_1 \Delta L}. \tag{9.10}$$

Generally, the waveguide parameters in the first and the second slab regions are the same; they are $D_1 = D$, $d_1 = d$, and $f_1 = f$. Then the channel spacings are the same as $\Delta\lambda_{in} = \Delta\lambda_{out} \equiv \Delta\lambda$. The path-length difference ΔL is obtained from Eqns (9.9) or (9.10) as

$$\Delta L = \frac{n_s\, dD\, \lambda_0}{N_c\, f\Delta\lambda}. \tag{9.11}$$

The spatial separation of the mth and $(m+1)$th focused beams for the same wavelength is given from Eqn (9.4) as

$$X_{FSR} = x_m - x_{m+1} = \frac{\lambda_0 f}{n_s d}. \tag{9.12}$$

X_{FSR} represents the free *spatial* range of AWG, which is also called the Brillouin zone width of the star coupler. The number of available wavelength channels N_{ch} is given by dividing X_{FSR} with the output waveguide separation D as

$$N_{ch} = \frac{X_{FSR}}{D} = \frac{\lambda_0 f}{n_s dD}. \tag{9.13}$$

Figure 9.16(a) and (b) shows a beam propagation method (BPM) simulation of the light-focusing property in the second slab region for the (a) central wavelength λ_0 and (b) a shorter wavelength component $\lambda < \lambda_0$. For the signal component which converges into the off-center output port as in Figure 9.16(b), higher or lower order diffraction beams appear. Because one of the two diffraction beams in

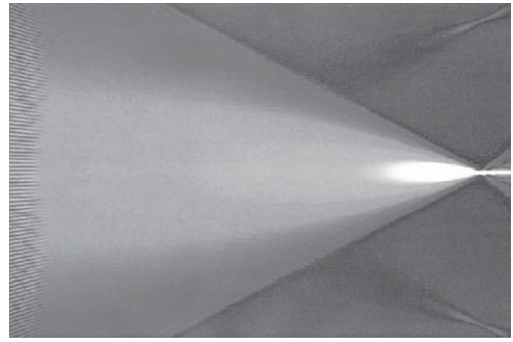

(a)

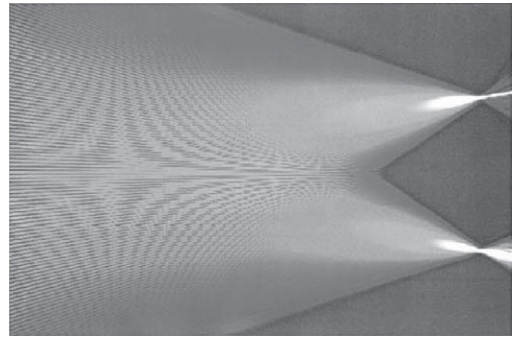

(b)

Figure 9.16 BPM simulation of the light-focusing property in the second slab region (rotated −90° from Figure 9.1) for the (a) central wavelength λ_0 and (b) shorter wavelength component $\lambda < \lambda_0$.

Figure 9.16(b) is usually thrown away, the insertion loss for the peripheral output port becomes $2 \sim 3$ dB higher than that for the central output port.

For further reading on AWG fundamentals see Refs [16–19].

Gaussian Spectral Response AWG

Non-technical overview: AWGs are optical filters with passbands that pass a certain spectral portion and block others. A "Gaussian AWG" means that the passband shape has a Gaussian shape. A Gaussian shape means that the passband transmission is of the form $\exp\{-[(\mathrm{f}-\mathrm{f}_0)/\mathrm{f}_{bw}]^2\}$*, where* f *is frequency,* f_0 *is the center frequency, and* f_{bw} *is the bandwidth. A real AWG passband is not precisely Gaussian-shaped and instead has sidelobes. Many applications do not favor Gaussian-shaped passbands because if a signal must pass through many such passbands in series, such as in a long optical link with many add–drop nodes, the net passband gets narrower and narrower, eventually distorting the signal.*

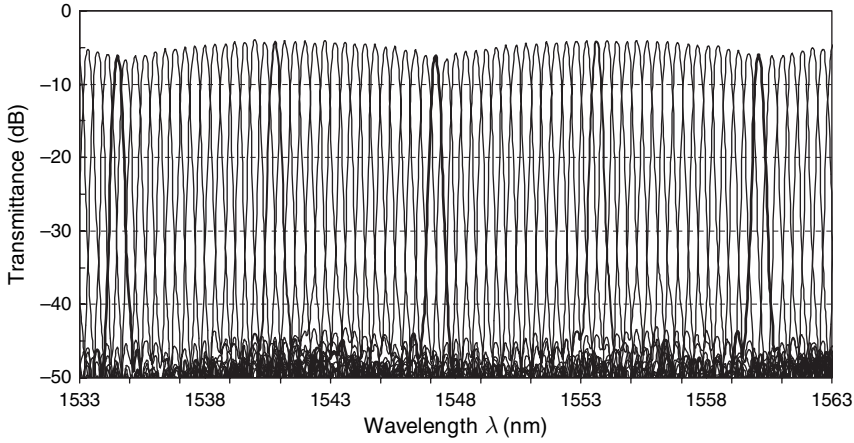

Figure 9.17 Demultiplexing properties of 32-ch 50-GHz spacing AWG over four diffraction orders.

A "Gaussian" AWG denotes that the frequency response has a Gaussian shape. Various kinds of multiplexers including a 50-nm-spacing 8-channel AWG and a 25-GHz spacing 400-channel AWG have been fabricated [20–22].

Figure 9.17 shows the measured transmission spectra of a 32-channel 50-GHz-spacing AWG over four diffraction orders. As explained by the BPM simulations in Figure 9.16(a) and (b), insertion losses for the peripheral output ports are $2.5 \sim 3$ dB higher than those for central output ports. In order to obtain uniform loss characteristics in WDM system applications, the total number of channels N_{ch} of AWG should be significantly larger than the channel number N_{system} of the system. The number of output ports N_{system} is usually $0.5 \sim 0.6 \times N_{\mathrm{ch}}$ to guarantee a loss variation of less than 1 dB.

Figure 9.18 shows the demultiplexing properties of a 400-channel, 25-GHz-spacing AWG. Crosstalk levels of about -30 dB have been achieved. Super-high-Δ waveguides with a refractive-index core-cladding contrast of 1.5% were used in the 400-channel 25-GHz AWG so as to minimize the area of the array waveguide region. Figure 9.19 shows the demultiplexing properties of a 32-channel AWG with a very narrow channel spacing of 10 GHz without using post processing for the phase-error (non-uniformity in the optical path-length difference $N_c \Delta L$) compensation. Here, a high-Δ waveguide with refractive-index difference of 0.75% was used. Adjacent channel crosstalk of approximately -30 dB has been achieved even in the 10-GHz spacing AWG. Postfabrication phase-error compensation techniques can further improve the crosstalk of AWGs.

AWG Crosstalk The crosstalk of an AWG is mainly attributed to the phase (optical path length) fluctuation in the arrayed waveguides [17]. If there were no phase (or amplitude) errors, we could obtain about a -60-dB level in the example

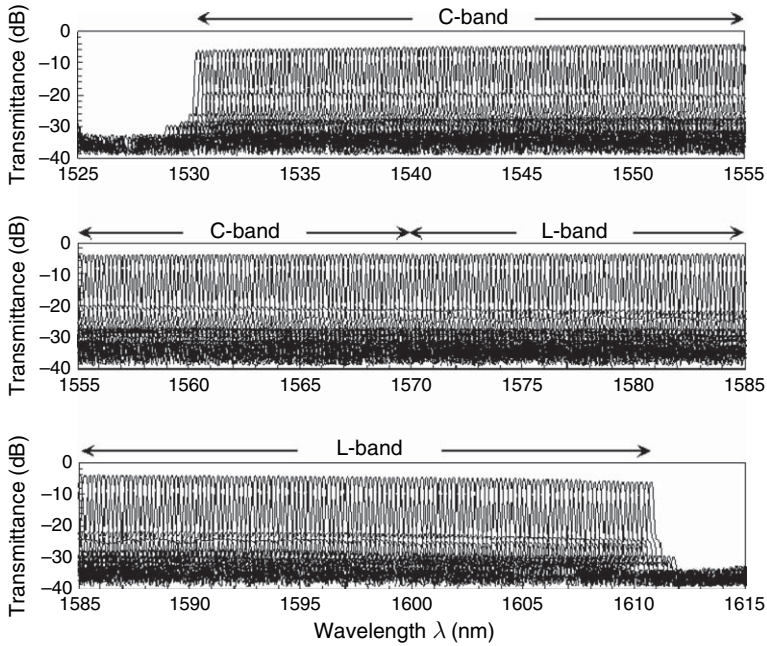

Figure 9.18 Demultiplexing properties of 400-ch 25-GHz-spacing AWG.

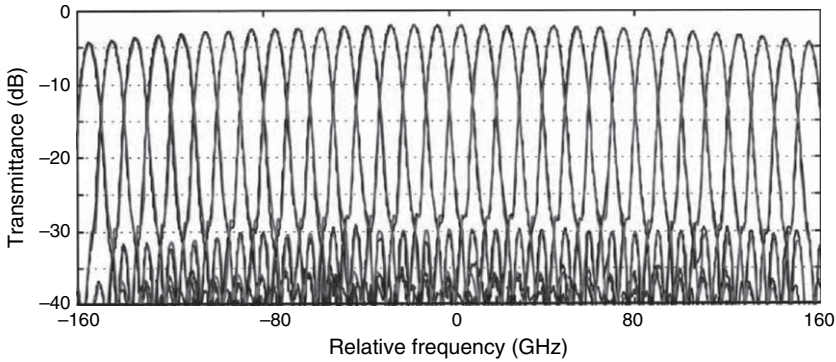

Figure 9.19 Demultiplexing properties of 32-ch 10-GHz-spacing AWG (this figure may be seen in color on the included CD-ROM).

with $\delta n = 0$ in Figure 9.20. The reason why we cannot achieve such a low crosstalk level in reality is that the envelope of the electric field at the second slab interface does not have a smooth Gaussian shape, because of phase errors in the AWG arms. Phase errors are caused by effective-index non-uniformities in the arrayed waveguide region; that is, refractive index fluctuations and core width and thickness non-uniformities. Excitation of higher order waveguide modes in the grating arms

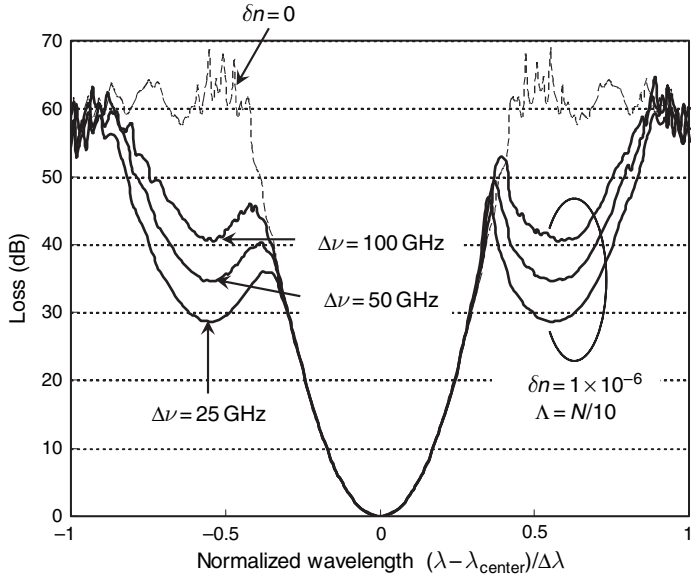

Figure 9.20 Theoretical demultiplexing properties of AWGs having sinusoidal phase fluctuation of $\delta n = 1 \times 10^{-6}$ with $\Lambda = N/10$ for three kinds of AWGs with 100-, 50-, and 25-GHz channel spacing.

can also cause phase errors. Figure 9.20 shows the demultiplexing properties of AWGs having sinusoidal phase fluctuations of $\delta n = 1 \times 10^{-6}$ with $\Lambda = N/10$ for three kinds of AWGs with 100-, 50-, and 25-GHz channel spacing, respectively. The spatial sinusoidal phase fluctuation is expressed by

$$\tilde{n}_c(\ell) = n_c(\ell) + \delta n(s) \cdot \sin\left[\ell \frac{\pi}{\Lambda(s)}\right] \tag{9.14}$$

where ℓ is an integer from 1 to N, and s denotes array number and order of spatial frequency in fluctuation, $n_c(\ell)$ is the ideal effective-index distribution, δn is an amplitude of fluctuation, and Λ is a half period of index fluctuation, respectively. It is known empirically that crosstalk degrades by $\sim$5 dB when the channel spacing is cut in half. It is also known that crosstalk degrades by $\sim$10 dB when δn becomes about 3.2 $(\sqrt{10})$ times larger.

AWG Dispersion Phase errors cause not only crosstalk but also chromatic dispersion in the AWG [23]. Figure 9.21 shows theoretical dispersion properties for 64-channel 100-GHz spacing to 64-channel 25-GHz spacing AWGs having spatially sinusoidal phase fluctuations given by Eqn (9.14). It is shown that a spatially low-frequency phase fluctuation (small s) causes dispersion inside the passband of AWG. Here, dispersion values are fixed to be -15 ps/nm in Figure 9.21(a)–(c) and

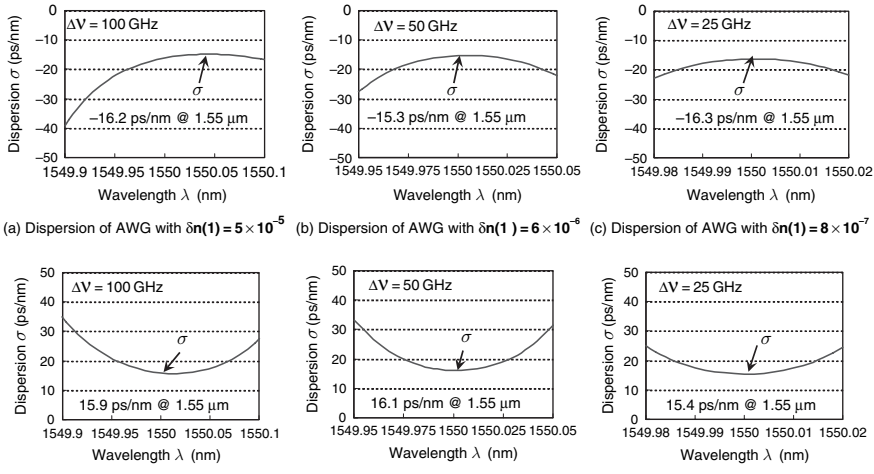

Figure 9.21 Theoretical dispersion characteristics of three kinds of AWGs with 100-, 50-, and 25-GHz channel spacing for various kinds of index fluctuation δn (this figure may be seen in color on the included CD-ROM).

$+15$ ps/nm in Figure 9.21(d)–(f), respectively. Then the index fluctuation δn that generates the specified dispersion is calculated. It is known empirically from several calculations including Figure 9.21 that the dependence of dispersion σ on index fluctuation δn and channel spacing $\Delta\nu$ is approximately obtained as $\sigma \propto \delta n/\Delta\nu^3$. Because σ is inversely proportional to $\Delta\nu^3$, the dispersion of an AWG with a narrow channel spacing is highly sensitive to phase errors.

Flat Spectral-Response AWGs

Non-technical overview: When multiplexing WDM channels together or demultiplexing them apart, one usually wants the optical passbands of the (de)multiplexer to have a magnitude vs wavelength that looks like a rectangle and a phase vs wavelength that is a straight line. This puts no distortion on a signal that is completely within the rectangle and filters out all noise outside of the rectangle. Such passbands are usually called "flat" passbands, and (de)multiplexers with such passbands are often called "wide-band" (de)multiplexers.

Because the rate of displacement of the focal position x with respect to the wavelength λ is constant [Eqn (9.7)], the transmission loss of a Gaussian AWG monotonically increases around the center wavelength of each channel. This places tight restrictions on the wavelength tolerance of laser diodes and requires accurate temperature control for both the AWGs and the laser diodes. Moreover, because optical signals may be transmitted through several filters in the WDM ring/bus networks, the cumulative passband width of each channel becomes much narrower than that of a single-stage AWG filter. One solution is to make the

Gaussian AWG passband very wide compared to the channel spacing, as discussed in Section "Gaussian Spectral Response AWG." This may be acceptable when the AWG is used as a multiplexer. However, it is not acceptable when the AWG is used as a demultiplexer, because of high crosstalk due to overlapping adjacent passbands. Therefore, flattened and broadened spectral responses with steep spectral skirts (i.e., a rectangular passband) are often required for AWG demultiplexers.

Several approaches have been proposed to flatten the passbands of AWGs [24–29]. One is to create a flat electric field distribution at the input waveguide. Because the AWG is an imaging device, the flat electric field is reproduced at the output plane. The overlap integral of a flat field with a Gaussian local normal mode gives a flat spectral response. Parabolic waveguide horns [25] or 1×2 MMI couplers [26] are used to create a flat electric field distribution at the input waveguide. The second method is to engineer array waveguide design to create a flattened electric field at the output plane. In this case, the input field is a normal Gaussian distribution. There are mainly two kinds of methods. One is to make a sinc-like electric field envelope in the array waveguides [24]. Because the focused electric field profile is a Fourier transformed image of the electric field in the array waveguides, we can generate a flattened field distribution at the output plane. The other is to make two focal spots at the output plane [27]. Here, the light-focusing direction of the array waveguide is alternately changed to two separate focal positions. In this case, the flattened field profile consists of two Gaussian beams.

All the above techniques pay a penalty in insertion loss by flattening the passband. There are some other flattening techniques employing concatenated interferometers that theoretically do not pay any loss penalty [28, 29]. In these techniques, the input position of the beam moves synchronously with the wavelength change of the signal, and they are discussed in Section "AWGs with Periodic Stationary Imaging." Then the output beam lies in a fixed position independent of wavelength within one channel span.

One way to create a flat spectral-response AWG is to place a non-adiabatic parabolic horn taper on the input waveguide at the first star coupler. The width of the parabolic horn along the propagation direction z is given by [30]

$$W(z) = \sqrt{\frac{2\alpha\lambda}{n_c}\, z + D^2}$$

where α is a constant less than unity and D is the core width of the channel waveguide. At the proper horn length $z = \ell$ less than the collimator length, a slightly double-peaked intensity distribution can be obtained as shown in Figure 9.22. A broadened and sharp-falling optical intensity profile is obtainable by the parabolic waveguide horn, which is quite advantageous for achieving a wide passband without deteriorating the nearest neighbor crosstalk characteristics. The broadened and double-peaked field is imaged onto the entrance of an output waveguide having a normal core width. The overlap integral of the focused field

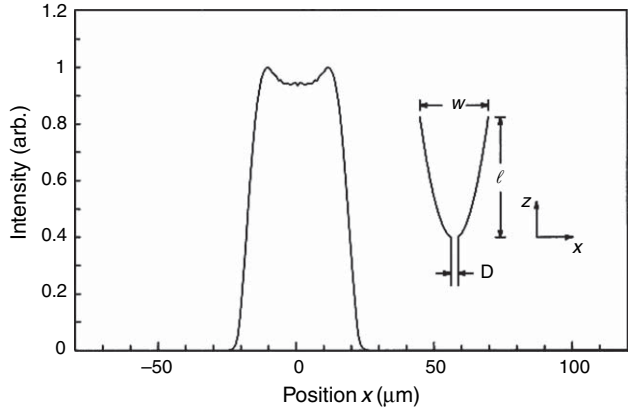

Figure 9.22 Intensity profile calculated by the beam propagation method in the parabolic input waveguide. Inset shows the schematic configuration of parabolic waveguide.

with the local normal mode of the output waveguide gives a flattened spectral response for the AWG. Figure 9.23 shows the demultiplexing properties of a 32-channel 100-GHz-spacing AWG having parabolic horns with $W = 26.1\,\mu\text{m}$ and $\ell = 270\,\mu\text{m}$.

In a parabola-type flat AWG, the double-peaked electric field distribution is created by the interference of the fundamental mode and the second order mode. Generally, phase retardations of the fundamental mode and second order mode are different. Therefore, the total phase at the end of the parabolic waveguide horn is not a uniform phase distribution. A non-uniform phase distribution in the parabola

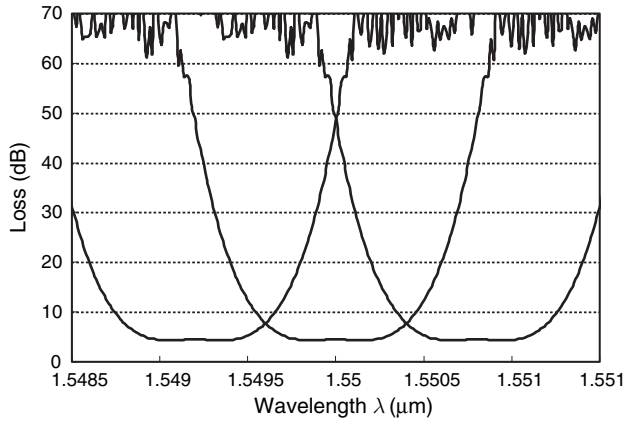

Figure 9.23 Demultiplexing properties of 32-ch 100-GHz-spacing AWG having parabolic horns with $W = 26.1\,\mu\text{m}$ and $\ell = 270\,\mu\text{m}$.

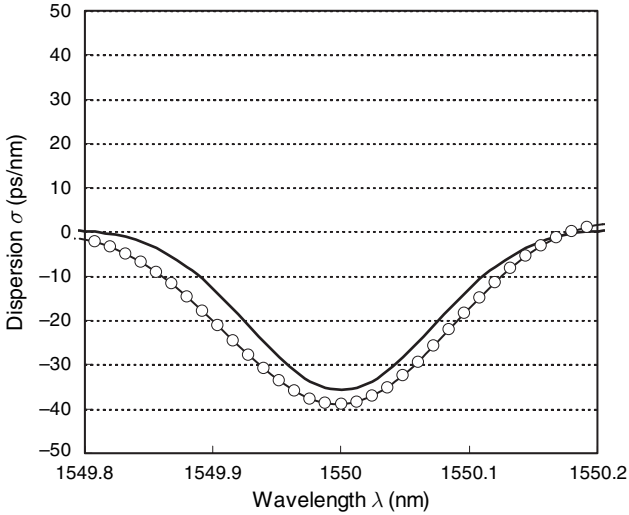

Figure 9.24 (a) Theoretical and (b) experimental dispersion characteristics of 32-ch 100-GHz parabola-type flat AWG.

input waveguide causes non-uniformity of phase in the array waveguides. It is known that the non-uniform phase is similar to the effective-index fluctuations in the array waveguides and thus can cause chromatic dispersion as described in the previous section. Figure 9.24 shows theoretical and experimental dispersion characteristics of a 32-channel 100-GHz parabola-type flat AWG.

Phase retardations between the fundamental and second order modes at the end of the parabolic waveguide horn can be adjusted by adding a straight multimode waveguide as shown in Figure 9.25 [31]. At the proper multimode waveguide length, phase retardations of the fundamental and second order modes are almost equalized. The total phase distribution becomes uniform while the double-peaked electric field distribution is maintained. Theoretical and experimental dispersion characteristics of 32-ch 100-GHz parabola-type flat AWG with $W = 26.1\,\mu\text{m}$, $\ell = 270\,\mu\text{m}$, and $L_{\text{multi}} = 85\,\mu\text{m}$ are shown in Figure 9.26. Chromatic dispersion has been reduced to a negligible value.

AWGs with Periodic Stationary Imaging *Non-technical overview: This section covers the concatenation of two or more interferometers, such as an MZI connected to an AWG or two AWGs connected together. By connecting multiple interferometers together, one can achieve a flat-top passband theoretically without introducing any extra loss.*

Achieving Multiple Zero-Loss Maxima How rectangular a passband is can be quantified by the number of maxima in the passband. For instance, a standard AWG has a Gaussian-shaped passband, which has one maximum in the passband.

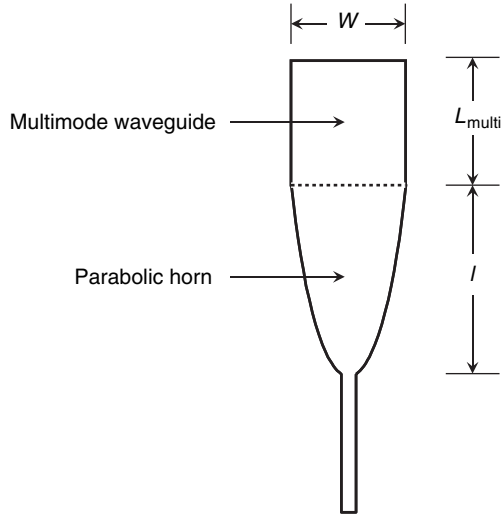

Figure 9.25 Parabolic waveguide having a straight multimode waveguide.

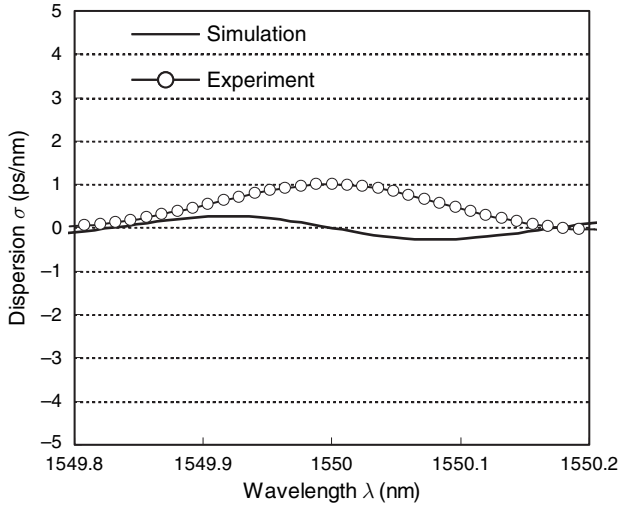

Figure 9.26 Theoretical and experimental dispersion characteristics of 32-ch 100-GHz parabola-type flat AWG with $W = 26.1\,\mu m$, $\ell = 270\,\mu m$ and $L_{multi} = 85\,\mu m$, respectively.

Such a passband is far from being rectangular. However, if we have two maxima in the passband, then the passband starts to look rectangular. The maxima in the passband can be at different frequencies or at the same frequency. When many of the same optical filter are placed in series, the net cascaded passband is simply a stretching of the scale of the passband, if it is plotted in dBs (in actuality, small

variation from filter to filter complicates this). For example, the 0.3-dB down point on the passband becomes the 3-dB down point after 10 cascades. The passband shape is stretched downward around the maxima. Thus, the more maxima (provided the maxima are at the same magnitude), the more the passband is "held open."

As shown in Section "Parabola-Type AWG," one way to add more maxima to an AWG passband is image mismatching, i.e., the image from the input waveguide does not match the image that an output waveguide would make. Such a method is compact and robust. However, image mismatching adds optical loss. This section addresses adding maxima without adding loss.

Any optical filter can be represented in the time domain by its impulse response, $u(t)$, and in the frequency domain by the Fourier transform of its impulse response, $\tilde{u}(f)$ (f is now frequency rather than star coupler length). For the discussion here, we will limit ourselves to directional optical filters that are periodic, with a free-spectral range (FSR) equal to Δf. Actually, any optical filter that is based on interference of different paths has a finite FSR. The time-domain impulses of such a filter are spaced by $1/\Delta f$.

$$u(t) = \sum_{k=1}^{K} c_k \delta\left(t - \frac{k}{\Delta f}\right) \tag{9.16}$$

$$\tilde{u}(f) = \sum_{k=1}^{K} c_k \exp\left(j2\pi k \frac{f}{\Delta f}\right) \tag{9.17}$$

where K is the number of impulses in the impulse response. If a filter has one zero-loss maximum per FSR, then the sum of the magnitudes of the impulses (in optical amplitude, not power) is equal to unity. Each impulse rotates in phase as the optical carrier frequency is changed, and they are all in phase once per FSR.

$$\sum_{k=1}^{K} |c_k| = 1 \quad \text{for one zero-loss maximum per FSR.} \tag{9.18}$$

If a filter has more than one zero-loss maximum per FSR, then this sum must be greater than unity. Otherwise, all the impulses must be in phase to achieve unity, and this can happen only once per FSR.

$$\sum_{k=1}^{K} |c_k| > 1 \quad \text{for multiple zero-loss maxima per FSR.} \tag{9.19}$$

Consider an arbitrary optical filter structure consisting of couplers and path lengths. If it has multiple zero-loss maxima per FSR, then the sum of the impulse magnitudes

must be greater than unity, as we just discussed. Now suppose we adjust the phases of all the various path lengths in any manner we choose. It must be impossible for us to put all the impulses in phase at any frequency, or else, we will violate the conservation of energy. Consider a case in which all the couplers in this optical filter structure are only $1 \times N$ and $N \times 1$ couplers, where N is any integer and can vary from coupler to coupler. If so, then at all the gathering couplers (i.e., all the $N \times 1$ couplers), we can adjust the phase of the input waveguides to these couplers such that the impulses exiting the coupler are all in phase. If the input to a gathering coupler is a sequence of impulses generated by other couplers, then all the impulses in that sequence have been put in phase by the preceding couplers. Subsequently, all the impulses exiting the filter can be adjusted to be in phase. Thus, an optical filter containing only $1 \times N$ and $N \times 1$ couplers cannot have more than one zero-loss maxima per FSR. Thus, we have proven the following theorem:

Flat-Top Filter Construction Theorem: a filter comprising couplers and connecting paths can have more than one zero-loss maximum per FSR only if at least one coupler is an effective $M \times N$ coupler, with M and $N > 1$.

By effective, we mean that coupler ports that are not used in a connection between a specified input and a specified output of the filter are disregarded. For example, for an MZI consisting of a 1×2 and a 2×2 coupler, the 2×2 coupler is effectively a 2×1 coupler, because we look at only one output port of the 2×2 coupler at a time. Also, if a coupler is connected to another one with equal path lengths, then those two couplers can be viewed as a single effective coupler. For example, if a 1×2 coupler is connected with equal path lengths to a $2 \times N$ coupler, then that structure can be viewed as a $1 \times N$ coupler.

Figure 9.27(a) and (b) shows examples of filters that can have at most one zero-loss maxima per FSR, and Figure 9.27(c) and (d) shows some that *may* have multiple zero-loss maxima per FSR. One will notice that Figure 9.27(a) is a conventional AWG.

A practical example of a filter with multiple zero-loss maxima per FSR is the Fourier filter interleaver, shown in Figure 9.28. This filter uses effective 2×2 couplers. One stage, shown as Circuit 1, has a nonlinear phase response, though. This can be overcome by cascading two identical filters in series, in which one connects one port of the first filter to the complementary port of the second filter [32]. This works because in a 2×2 filter, the amplitude transmissivity from one input port to one output port is equal to the complex conjugate of the amplitude transmissivity between the other input port to the other output port. The next section shows a multiple zero-loss maxima filter that has a linear phase response without needing two stages.

AWG with Two-Arm-Interferometer Input Based on the theorem just proven, we realize that a conventional AWG can have only one zero-loss maximum per FSR. In this Section, we create an AWG with two zero-loss maxima per FSR. To do this, we will have to connect the device input to more than one input of

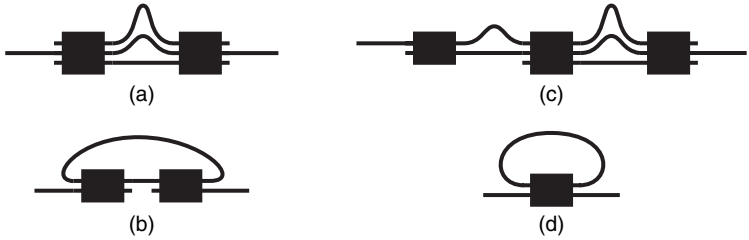

Figure 9.27 Example of optical filter designs. (a) and (b) cannot have multiple zero-loss maxima per FSR, because they contain only effective $1 \times N$ or $N \times 1$ couplers. (c) and (d) may have multiple zero-loss maxima [(d) actually has an infinite number of zero-loss maxima], because (c) contains an effective 2×3 coupler, and (d) contains an effective 2×2 coupler.

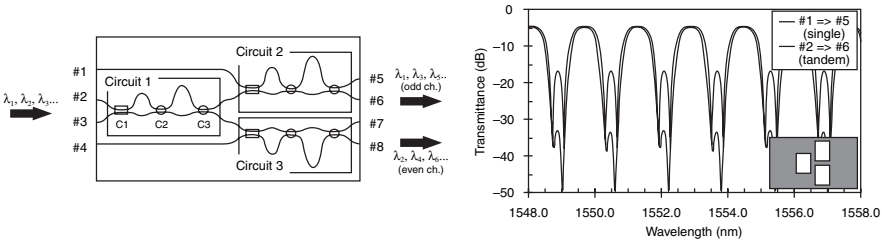

Figure 9.28 Fourier filter-based interleaver and concept for achieving zero dispersion with 2×2 filters. As one can see, the port-pair combination in the left stage is complementary to the port-pair combination in the right stage.

the first AWG star coupler (or equivalently connect the device output to more than one output from the second AWG star coupler) with different path lengths in the connections.

To figure out what to connect between the device input and the two star coupler inputs note that the problem with a conventional AWG is that the image in the second star coupler is always moving as wavelength increases. To create two zero-loss maxima per FSR, we need to have the image focus on the output waveguide in the second star coupler twice per FSR. To do this, we need to move the image in the first star coupler as wavelength changes. We can accomplish this by having a length-imbalanced MZI connected to the two inputs of the first star coupler, where the light moves from one input to the second as wavelength changes such that both images focus on the same output waveguide [29, 33]. If we then match the FSR of the MZI to the channel spacing of the AWG, then one MZI can create dual zero-loss maxima for all channels.

Figure 9.29 shows a plot of the optical power from the MZI at the MZI—star coupler junction as the wavelength changes. The light switches from one output to the other. In between these states, the light is in both outputs simultaneously. One can view the "center of mass" of the optical distribution as moving continuously

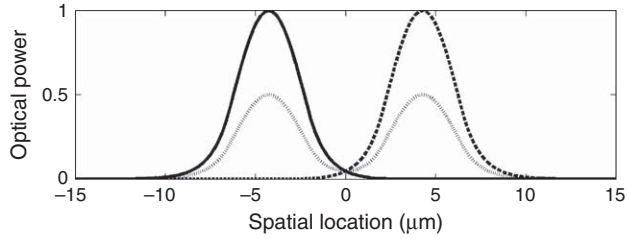

Figure 9.29 Change in optical field at end of a length-imbalanced MZI with a directional 2×2 coupler as the optical frequency is changed.

between the two states. Because this is imaged by the AWG onto the output waveguide, one can view the MZI as making the center of mass of the image stationary on the output waveguide. This is what creates the desired low-loss flat-top passband.

Two possible ways of laying out the MZI–AWG are shown in Figure 9.30. Figure 9.30(a) shows the MZI and AWG having the same sign of "curvature." This is necessary for the synchronization of the MZI and AWG at their interconnection point. Figure 9.30(b) shows a switching of the sign of curvature. This is possible by having a sort of waveguide crossing in the MZI, effected by using a 100/0 coupler. It is found that a relative phase shift of 180° between the waveguides between the 100/0 coupler and the 50/50 coupler minimizes the performance sensitivity to wavelength, fabrication, and polarization changes.

Figure 9.31 shows an actual waveguide layout and the resulting measured transmissivity. Theoretically, the chromatic dispersion in the passband is zero.

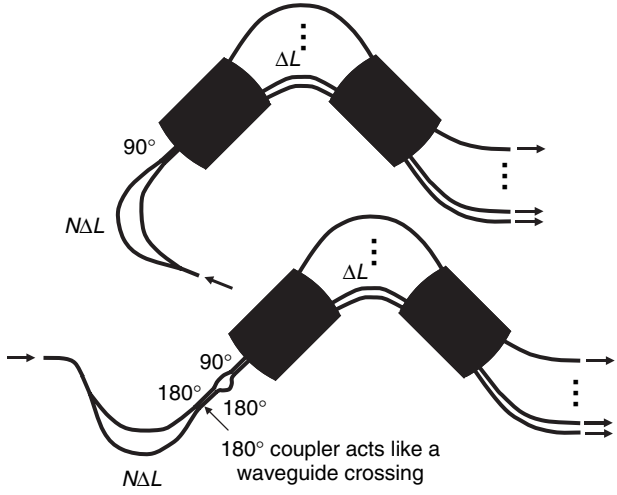

Figure 9.30 Possible layouts for a rectangular passband demultiplexer consisting of an MZI directly connected to an AWG (this figure may be seen in color on the included CD-ROM).

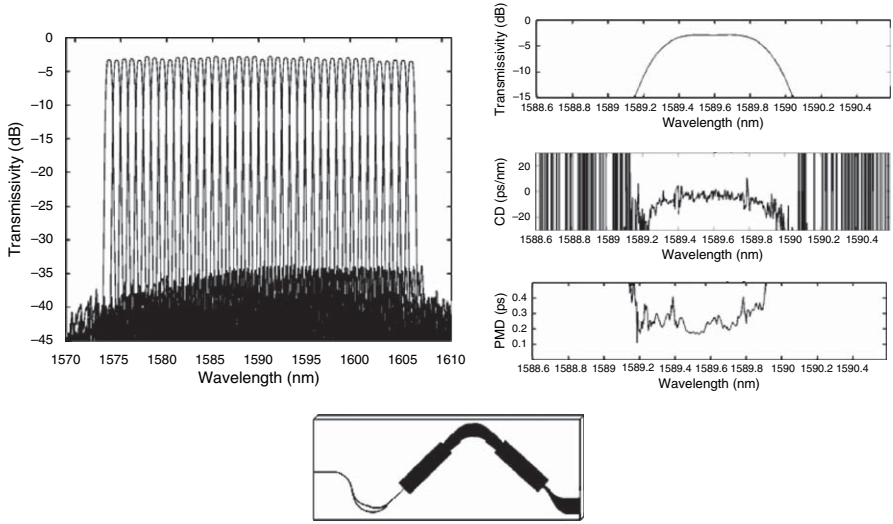

Figure 9.31 Waveguide layout and measured results from a demultiplexer consisting of an MZI directly connected to an AWG.

However, if the 50/50 coupler has a splitting ratio error, then the device will exhibit dispersion. This can be understood by following a signal passing from right to left through the device. Suppose the 50/50 coupler is too weak. Then, when the signal from the AWG is imaged onto the upper waveguide of the 50/50 coupler, which is the short-wavelength side of the passband, then instead of the signal being divided evenly between the two MZI arms, more light will be coupled to the longer MZI arm. The effective path length through an interferometer is equal to the average of the path lengths weighted by the optical power in each arm. Thus, the total path length through the device will be longer on the shorter wavelength side of the passband. It will be vice versa for the longer wavelength portion. Thus, the passband will exhibit negative dispersion.

AWG with Three-Arm Interferometer Input We just showed how to create a passband with two zero-loss maxima by connecting a two-arm interferometer to an AWG. One can extend this principle by using a larger number of arms in the input interferometer. However, some challenges arise once the number of arms is greater than two. Here, we address them for an arm number of three [34, 35].

The main challenge with going from two to three arms is the directional coupler that connects to the AWG. As we will show, a three-arm directional coupler is not trivial, and it has an undesirable phase relationship between the outputs. One might think why not turn the input interferometer into a small AWG and use a star coupler? However, a star coupler with a low port count (approximately <8) has a very low efficiency, undoing our intent of making a low-loss flat-top passband.

A star coupler with a low port count has a low efficiency because the waveguides converge too quickly to convert the plane waves of the free-space region to only first-order Bloch modes of the waveguide array.

The problem with the three-waveguide directional coupler is that the difference of the phase between adjacent output waveguides from the coupler when illuminating one input waveguide of the coupler is always an integer multiple of 90°, whereas we would like it to be an integer multiple of 120°. We would like it to be 120° because this is the phase difference encountered in an ideal star coupler, and it is a star coupler that creates a linearly moving image. The phase between port m_1 on one side and m_2 on the other side of an ideal $M \times M$ star coupler is

$$\phi = \frac{2\pi}{M}\left(m_1 - \frac{M+1}{2}\right)\left(m_2 - \frac{M+1}{2}\right) \tag{9.20}$$

For $M = 3$, one can see that this gives either 0° or 120° phase difference. The 90° phase difference encountered in the directional coupler means that the three passbands per FSR from the input interferometer are unequally spaced in frequency, and the resulting interferometer-plus-AWG device exhibits mostly a two zero-loss maxima passband. However, using a multi-section three-waveguide directional coupler, one can achieve the desired phase difference and achieve a three zero-loss maxima passband. The design and results are shown in Figure 9.32.

If we wish to use more than three arms and not use a star coupler for the second coupler of the input interferometer, then we have a difficult problem with the design of the input interferometer. As shown in Ref. [36], if one makes a demultiplexer using an MMI coupler (and likewise with a directional coupler), the arm lengths no longer follow a linear progression in path length when the arm number is greater than three.

AWGs with High Spectral Sampling

Non-technical overview: An AWG demultiplexer has a passband for each output port, the passband shifted in wavelength from port to port. If the passbands are very narrow compared with their spacing, then the spectral sampling of the AWG is low. If the passbands are very wide compared with their spacing (they can even be wider than the spacing in some designs), then the spectral sampling is high. If the passbands are about the same width as their spacing, then the spectral sampling is about 1.0.

Suppose we have a conventional AWG with one input and N outputs, and we launch a signal into the input. The N outputs take discrete "samples" of the spectrum of the input signal, spaced in spectrum by a certain amount and "filtered" by a

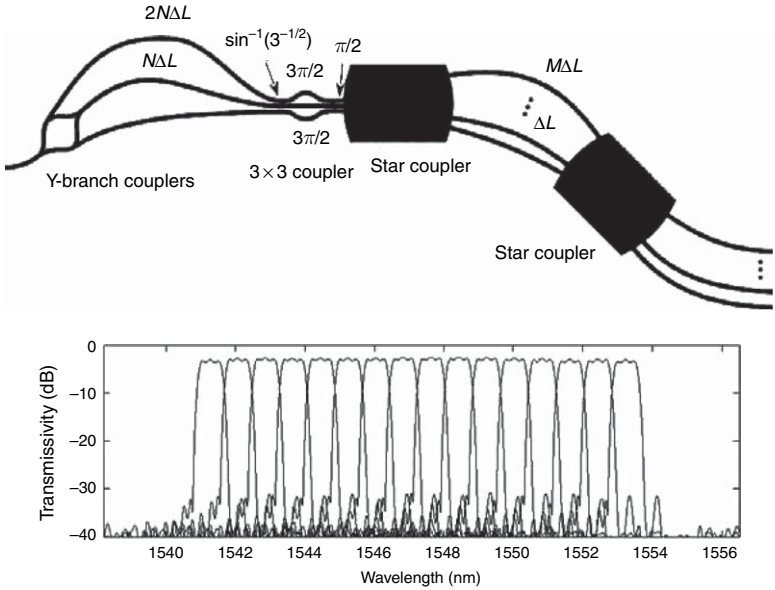

Figure 9.32 16-Channel demultiplexer consisting of a three-arm interferometer directly connected to an AWG. (a) schematic and (b) measured passbands.

certain "bandwidth" [37]. This is analogous to sampling in the time domain, in which a waveform is sampled by discrete-time sample points spaced in time by a certain amount and filtered by a certain "bandwidth."

Sampling Theorem For the time-domain case, if a spectrum is zero for frequency $|f| > f_B/2$, and the signal is sampled in time by spacing T, then we can define a sampling coefficient

$$s = \frac{1}{Tf_B}. \tag{9.21}$$

The sampling theorem states that if $s \geq 1$, then the signal is uniquely determined by its samples.

We can derive a similar relation for the AWG in the spectral domain. The field along one edge of a star coupler is approximately the spatial spectrum (i.e., Fourier transform) of the field along the other edge. The output waveguides of the AWG are thus sampling the spatial spectrum of the field from the grating arms. If we make this field from the grating arms zero outside of a spatial width w, and if the output waveguides are spaced closely enough, then the samples in the output waveguides can uniquely determine the field along the grating arm edge of the

output star coupler in the AWG. This field is determined by the input signal spectrum. Thus, we can uniquely determine the input spectrum by these discrete samples. To make the field zero outside of width w, we can simply use a limited number of grating arms in the AWG. $w = Ma$, where M is the number of grating arms, and a is the grating arm pitch at the connection to the output star coupler. Note that the star coupler can still have dummy waveguides outside of width w, to which the field can couple, because the dummy waveguides are necessary for the star coupler to perform an accurate Fourier transform.

If the output waveguides have pitch b at their connection to the output star coupler, then the sampling coefficient is

$$s = \frac{R\lambda}{Mab}, \tag{9.22}$$

where R is the star coupler radius (called f in earlier sections in this chapter), and λ is the wavelength in the slab (i.e., not the free-space wavelength). Thus, if $s \geq 1$, the information in the output waveguides is sufficient to uniquely determine the AWG input signal. Note that because there are a finite number of output waveguides, the signal time-frequency spectrum must be band-limited for this to be true. It is analogous to the time-domain case, in which the signal must be limited in its time extent because only a finite number of time-sampling points can be recorded.

Interestingly, when $s = 1$, the output star coupler is an $M \times M$ star coupler, although it is possible that less than M output waveguides are actually used.

One use for an AWG with high sampling is as a multiplexer with very wide passbands and no concern for crosstalk level. Other uses including making a dynamic gain equalization filter (DGEF) and a band de/multiplexer, described later in this section.

Aberrations A conventional Gaussian-passband AWG demultiplexer has $s \approx 0.5$. As s is increased toward one and beyond, a significant problem in the AWG usually develops: the output waveguides become so close that there is significant mutual coupling between them. If left uncorrected, this results in aberrations that give high loss and large passband shoulders. To mitigate the mutual coupling, one could increase b. However, this results in a longer R [see Eqn (9.22)] and a larger device size. An alternative solution is to move the aiming point of the grating waveguides into the output waveguides and then slightly modify the grating arm path lengths [38].

To calculate how much to adjust the grating arm lengths, one must calculate the transmissivity from each grating waveguide through the second star coupler to each output waveguide and use the phase of the transmissivity to adjust the grating arm lengths. When there is mutual coupling between the waveguides, a useful tool is BPM. Many types of BPM exist, such as Fourier transform BPM (FT-BPM) and finite-difference BPM (FD-BPM). FT-BPM can handle wide angles, but is slow

and cannot handle large index steps. FD-BPM is much faster and can handle large index steps, but cannot handle wide angles. There is another type called sinc-BPM [39], which is based on FT-BPM, but stays in the angular spectrum domain. It is fast and accurate for periodic waveguide arrays, found, for example, in star couplers.

To calculate the transmissivities mentioned earlier, we first calculate the waveguide mode of a grating waveguide at a point that is far enough away from the slab region as to be uncoupled to other grating waveguides. Then we use BPM to propagate it until it reaches the slab boundary. Call this field u_1. Then we likewise calculate the waveguide mode in an output waveguide at a point far from the slab region and use BPM to propagate it until it reaches the slab boundary. Call this field u_2. The transmissivity through the second star coupler in an AWG from a grating waveguide at angle θ_1 to an output waveguide at angle θ_2 is

$$t(\theta_1, \theta_2) = \frac{\int_{-\infty}^{\infty} u_1^{\text{prop}}(x) u_2(x) \exp[\mathrm{j}kx(\theta_2 - \angle AB)]\mathrm{d}x}{\sqrt{\int_{-\infty}^{\infty} |u_1(x)|^2 \mathrm{d}x \int_{-\infty}^{\infty} |u_2(x)|^2 \mathrm{d}x}} \tag{9.23}$$

$$AB = R\left(e^{-\mathrm{j}\theta_1} - 1 + e^{\mathrm{j}\theta_2}\right) \tag{9.24}$$

$$u_1^{\text{prop}}(x) = F^{-1}\left\{F\{u_1(x)\exp[\mathrm{j}kx(\theta_1 - \angle AB)]\}\exp\left(\mathrm{j}\sqrt{k^2 - k_x^2}|AB|\right)\right\} \tag{9.25}$$

$$F\{u(x)\} = \int_{-\infty}^{\infty} u(x) e^{\mathrm{j}xk_x} \mathrm{d}x \tag{9.26}$$

If there is no mutual coupling among the waveguides connected to the slab region, then $\angle t(\theta_1, \theta_2)$ is a linear function of θ_1 and θ_2. If there is mutual coupling, then the path lengths of the waveguides should be adjusted so as to make $\angle t(\theta_1, \theta_2)$ a linear function of θ_1 and θ_2.

In general, when designing a star coupler with mutual coupling between waveguides, it is best to aim for making u_1 and u_2 such that the power coupled to each of the two adjacent waveguides is $\sim$4 dB less than the power in the launched waveguide. Increasing the mutual coupling beyond this tends to make the device too sensitive to fabrication details.

Just as segmentation [40], vertical tapering [41], or selective UV exposure [42] (see Figure 9.33) improve the AWG grating efficiency, these techniques can also improve the coupling efficiency to highly sampled output waveguides. They work by reducing the abruptness of the transition from the waveguide array to the slab region. Segmentation is the easiest to implement because it does not require any extra fabrication steps. In segmentation, one simply adds sections (15 is a typical number) perpendicular to the waveguides. The section center-to-center

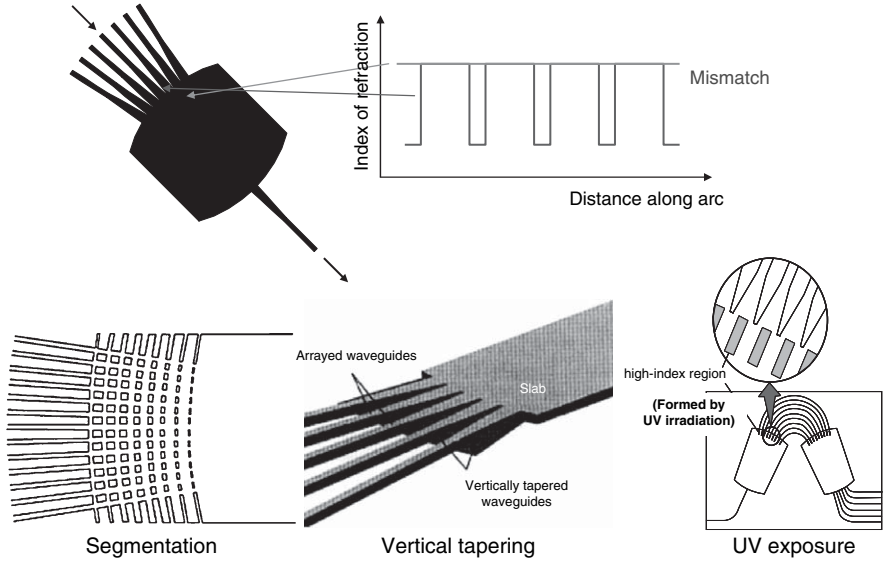

Figure 9.33 The upper figure shows the mismatch in refractive index distribution at the slab-to-array transition in a star coupler, which is a significant source of insertion loss in AWGs. The lower figures show various demonstrated schemes for reducing this loss (this figure may be seen in color on the included CD-ROM).

spacing is constant, but their widths gradually decrease as their distance from the slab increases.

Dynamic Gain Equalization Filter In Section "Achieving Multiple Zero-Loss Maxima," we proved that we need $N \times M$ couplers, where $N, M > 1$ to create a passband with more than one zero-loss maximum. In Sections "AWG with Two-Arm-Interferometer Input" and "AWG with Three-Arm Interferometer Input," we then showed how to make a two-maxima passband and a three-maxima passband by connecting two-arm and three-arm interferometers, respectively, directly to an AWG. Here, we connect one AWG to another AWG through an arrayed waveguide lens (AWL) to create a passband with numerous zero-loss maxima. By inserting either phase shifters or VOAs into the AWL arms, we create a dynamic filter that can control the channel powers in a WDM link, often called a DGEF [43].

An AWL is an AWG with a grating order of zero, i.e., the path lengths of all the arms in the "grating" are equal. In order to lay out such a structure without waveguides running into each other, the conventional "U"-shaped structure of an AWG cannot be used. Instead, it is best to use a "W"-shaped structure.

We would like the DGEF to be able to pass all the WDM channels in a given spectral region without any distortion. In order to do this, the AWL ports must

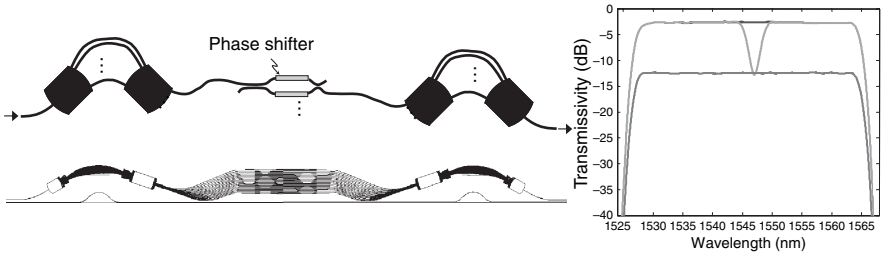

Figure 9.34 DGEF consisting of two AWGs connected by an AWL. Upper left is the concept, lower left is the actual waveguide layout (has 16 waveguides in the AWL), and the right is the measured response, fiber-to-fiber (this figure may be seen in color on the included CD-ROM).

perfectly or over sample the spectra from the AWGs, i.e., $s \geq 1$ for all AWL ports and all λ in the spectral region of interest.

A layout for a DGEF is shown in Figure 9.34. There is an MZI with thermooptic phase shifters in each arm. Each MZI must be driven in a push–pull fashion so as to maintain a constant phase difference between adjacent AWL arms. Using push–pull also reduces the polarization dependence, because it reduces the maximum required phase shift, and a typical silica thermooptic phase shifter shifts TM-polarized light 4% more efficiently than TE-polarized light. Furthermore, push–pull reduces the worst-case power consumption and keeps the total heat dissipation constant [43]. A measured spectral response through the DGEF is shown in Figure 9.34(b) when all VOAs are set for minimum attenuation, when one VOA is set for increased attenuation, and when all VOAs are set for increased attenuation. One can see that the spectral response is smooth and ripple-free, although the spectrum is broken into discrete sections by the AWGs.

There is another DGEF arrangement which has a lower insertion loss, which is shown in Figure 9.35. It consists of a large interferometer with one arm containing

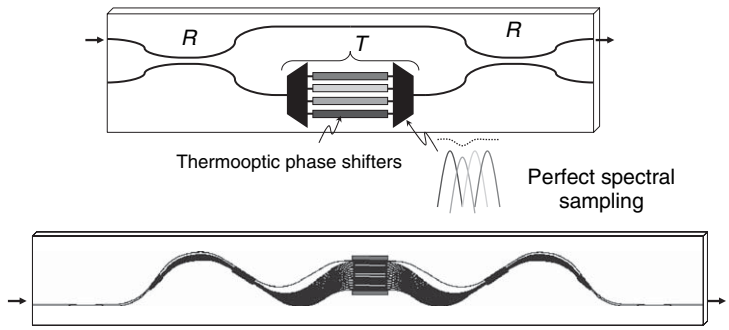

Figure 9.35 Lower loss DGEF using a large interferometer. Concept (upper) and actual waveguide layout (lower) (this figure may be seen in color on the included CD-ROM).

an AWG–AWL–AWG series [44]. In this DGEF, each AWL arm contains just a phase shifter rather than an MZI. The couplers of the interferometer do not have to have a 50/50 coupling ratio. The overall insertion loss is lower than the insertion loss of the AWG–AWL–AWG series because only a portion of the light passes through the AWG–AWL–AWG series. The main drawback to this design is that because of the large interferometer with different elements in each arm, it is difficult to make it insensitive to the environment and the input light polarization. One way to solve the polarization-dependence difficulty is to use polarization diversity.

Band Multiplexer With appropriate settings of the phase shifters, the DGEF can act as a band filter, a filter with a very wide passband and very steep sidewalls. With a small modification, one can change it into a band de/multiplexer (we will call it just a multiplexer from here on) [45]. The concept is shown in Figure 9.36. In this case, the AWL is split into groups at one end. Because each group enters the right-hand AWG at a different location, the spectral portions carried by each group are sent to different outputs. Note that in this design it is not necessary that the AWL arm path lengths be the same from group to group.

It is important to note that this band multiplexer does not exhibit any chromatic dispersion. This is because all path lengths are the same for all wavelengths (provided the aberrations have been compensated for). This is possible because AWG filters are non-minimum phase filters [46]. Thus, AWGs need not obey the Kramers–Kronig relations and so can have rectangular shaped passbands and linear phase simultaneously. This is unlike conventional band filters which are made from thin-film technology. Those band filters are made from a series of resonances and are infinite-impulse response filters. In transmission, thin-film filters are minimum phase filters and thus obey the Kramers–Kronig relations. These filters have significant dispersion at sharp passband corners, resulting in signal distortion.

A waveguide layout and measured results from a 5-band 8-skip-0 multiplexer are shown in Figure 9.37 [47]. A-skip-B means that each band carries A number of channels (typically on a 100-GHz grid), and there are dead zones of B channels between them. As expected, the chromatic dispersion is negligible, even at the passband corners.

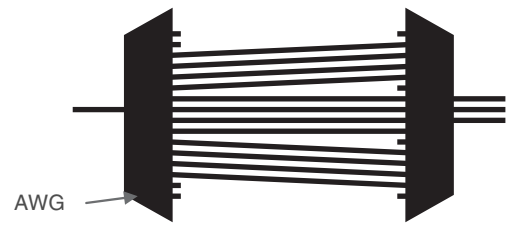

Figure 9.36 Concept of band de/multiplexer using AWGs (this figure may be seen in color on the included CD-ROM).

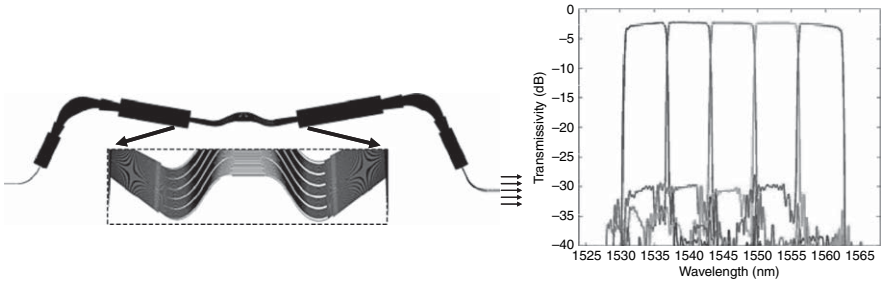

Figure 9.37 8-skip-0 5-band de/multiplexer (this figure may be seen in color on the included CD-ROM).

There is a type of WDM called coarse WDM (CWDM), which has a 20-nm channel spacing. The channel spacing is so wide because it is designed for non-temperature-controlled laser transmitters. The passbands for CWDM typically must be wide and flat with a bandwidth greater than 14 nm. The band multiplexer is a good way to make a CWDM de/multiplexer. Figure 9.38 shows a waveguide a layout for an 8-channel CWDM multiplexer and the measured response [48]. Because the channel spacing is so wide, the AWG grating orders are very small and having unequal path lengths in the AWL adds a negligible amount of

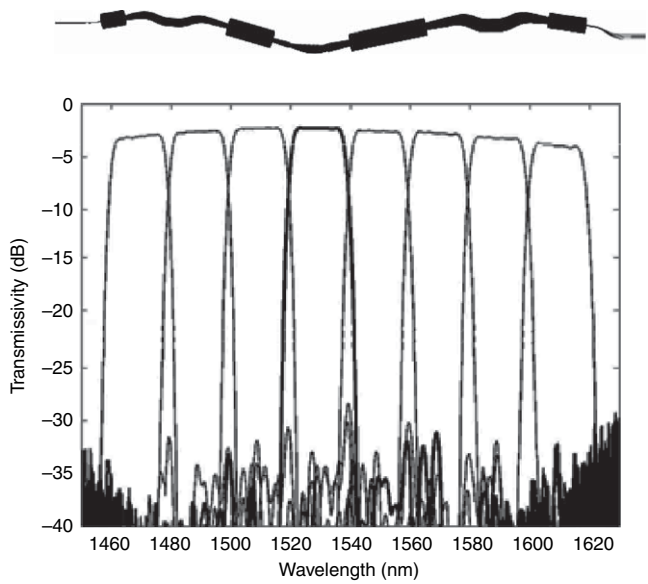

Figure 9.38 8-channel CWDM (de)multiplexer. Waveguide layout (upper) and measured passbands (lower).

chromatic dispersion (allowing one to use a "U" shape for the AWL, making it more compact). Thus, the AWGs take on a "W" shape, and the AWL takes on a "U" shape, the opposite of the case in Figure 9.37.

A highly compact silica waveguide PLC 4-channel CWDM multiplexer made using a completely different technique, a two-dimensional reflective hologram, is shown in Section 9.3.3.

Athermal (Temperature-Insensitive) AWGs

Non-technical overview: The refractive index of PLCs changes with temperature. This causes the filter response of PLCs to shift wavelength when their temperature is changed. The amount of shift depends only on the refractive index change with temperature and not the filter design itself. Silica PLCs shift approximately +0.01 nm/°C, InP and Si PLCs shift approximately +0.1 nm/°C, and polymer PLCs shift approximately −0.3 nm/°C. The shift is undesirable in DWDM systems. To avoid this, often the PLC is temperature controlled, using either a thermo-electrical cooler or a heater. Another approach is to make the PLC "athermal," the topic of this section.

The temperature sensitivity of the passband center wavelength (frequency) in the silica-based AWG is about $d\lambda/dT = 1.2 \times 10^{-2}$(nm/deg) [$d\nu/dT = -1.5$(GHz/deg)], which is mainly determined by the temperature dependence of silica glass itself [$d_{nc}/dT = 1.1 \times 10^{-5}(\text{deg}^{-1})$]. The AWG multiplexer should be temperature controlled with a heater or a Peltier cooler to stabilize the channel wavelengths. This requires a constant power consumption of a few Watts and significant equipment for the temperature control. Various kinds of AWG configurations to achieve athermal operation have been proposed [49–52].

Figure 9.39 shows a schematic configuration of an athermal AWG in which temperature-dependent optical path-length change is compensated by movement

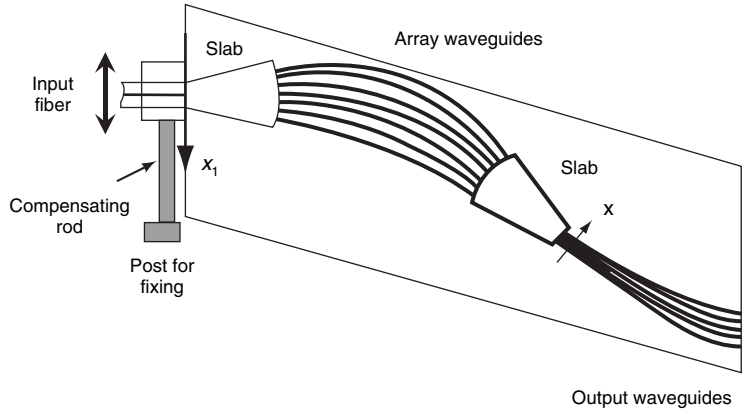

Figure 9.39 Configuration of an athermal AWG with a temperature compensating input position: From Ref. [49].

of the input fiber position. The input coupling device consists of three parts: namely one part holding the input fiber, an additional post to fix the whole coupling device to the chip, and a metal compensating rod between them. The compensating rod is made of a material with a high thermal expansion coefficient, aluminum. It changes its length with the ambient temperature T and shifts the input fiber along the endface of the slab waveguide to compensate for the thermal drift of the passband center wavelength in the AWG.

Figure 9.40 shows the shift of several channels' peak transmissions with temperature for a 200-GHz module. The temperature is varied from -35 to $+80$°C. The center wavelength of the AWG filter is nearly independent of the ambient temperature. This method may be applied to spectrographs and phased array filters realized in any material.

Figure 9.41 shows a schematic configuration of a completely solid-state athermal AWG. The temperature-dependent optical path difference in silica waveguides is compensated with a trapezoidal groove filled with silicone adhesive which has a negative thermooptic coefficient. Because the passband center wavelength is given by $\lambda_0 = n_c \Delta L/m$, the optical path-length difference $n_c \Delta L$

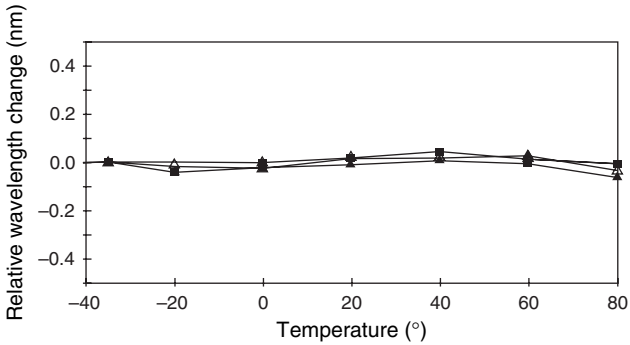

Figure 9.40 Temperature dependences of the passband center wavelengths.

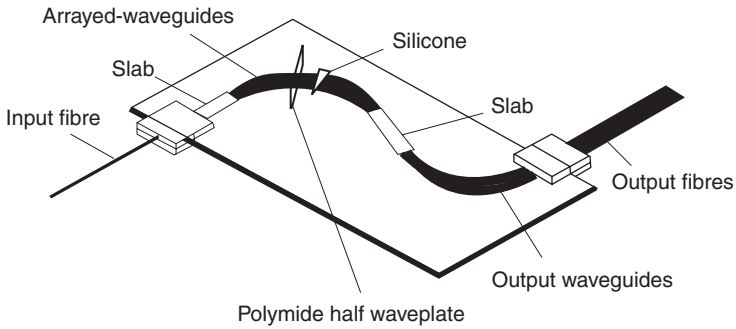

Figure 9.41 Schematic configuration of silicone-filled athermal AWG.

must be made insensitive to temperature. Therefore, the groove is designed to satisfy the following conditions

$$n_c \Delta L = n_c \Delta \ell + \hat{n}_c \Delta \hat{\ell}, \tag{9.27}$$

and

$$\frac{\mathrm{d}(n_c\ \Delta L)}{\mathrm{d}T} = \frac{\mathrm{d}n_c}{\mathrm{d}T}\Delta \ell + \frac{\mathrm{d}\hat{n}_c}{\mathrm{d}T}\Delta \hat{\ell} = 0, \tag{9.28}$$

where $\hat{n}$ is the refractive index of silicone and ΔL and $\Delta \hat{\ell}$ are the path-length differences of silica waveguides and silicone region, respectively. Equation (9.27) is a condition to satisfy the AWG specifications and Eqn (9.28) is the athermal condition, respectively. The temperature sensitivity of silicone is $\mathrm{d}\hat{n}_c/\mathrm{d}T = -37 \times 10^{-5}(\mathrm{deg}^{-1})$. Therefore, the path-length difference of silicone is $\Delta \hat{\ell} \cong \Delta \ell / 37$. Figure 9.42 shows temperature dependencies of passband center wavelengths in conventional and athermal silicone-groove-filled AWGs. The temperature-dependent wavelength change has been reduced from 0.95 to 0.05 nm in the $0 \sim 85$°C range. The excess loss caused by the groove is about 2 dB, which is mainly due to diffraction loss in the groove. The insertion loss caused by diffraction loss can be reduced by segmenting a single trapezoidal silicone region into multiple groove regions [53]. In the segmented groove regions, the light beam is periodically refocused and the insertion loss is reduced to about 0.4 dB.

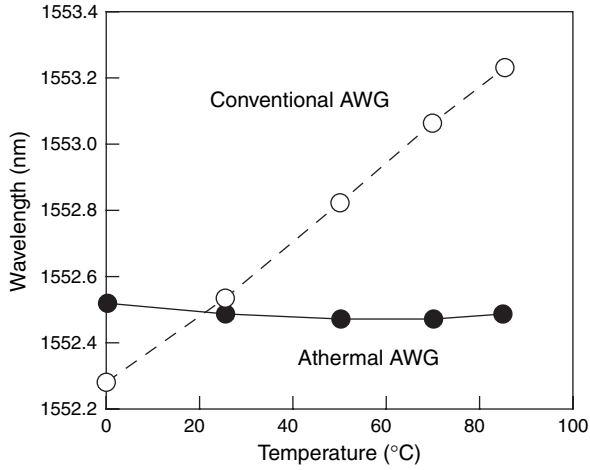

Figure 9.42 Temperature dependences of passband center wavelengths in a conventional AWG and a silicone-filled athermal AWG.

Tandem AWG Configuration

The maximum available wafer size of a PLC is limited by the fabrication apparatus such as the deposition machine, electric furnace, mask aligner, etc. Therefore, it is not easy to fabricate AWGs with very large channel counts. One possible way to increase the total number of channels is to use two kinds of AWGs, which are cascaded in series. These AWGs are connected with a single-mode connection and so have no relation to the periodic stationary imaging principle. Figure 9.43 shows the configuration of a 10-GHz-spaced 1010-channel WDM filter that covers both the C and the L bands [54]. It consists of a primary 1×10 flat-top AWG (AWG #k with $k = 1, 2, \ldots, 10$) with a 1-THz channel spacing and ten secondary 1×101 AWGs with 10-GHz spacing and 200 channels. Crosstalk levels of the secondary AWGs are around -32 dB, and the sidelobe levels in these passbands are less than -35 dB. The tandem configuration enables us to construct flexible WDM systems, that is, secondary AWGs can be added when bandwidth demand increases. Also, this configuration will be essential for the construction of hierarchical cross-connect (XC) systems such as fiber XC, band XC, and wavelength XC. Output port #k ($k = 1, 2, \ldots, 10$) of the primary AWG is connected to the input port of AWG #k through an optical fiber. Two conditions are imposed on these AWGs. First, the center wavelength of 200 channels of AWG #k should be designed to coincide with that of the flat-top passband #k from primary AWG output #k. Then, passband #k is sliced with the AWG #k without any noticeable loss. Second, the sidelobe components of flat-top passband #k are removed as shown in the inset of Figure 9.43. Therefore, one passband within the FSR is obtained from one output port of AWG #k. 101 wavelengths are selected from every AWG #k. Figure 9.44 shows the demultiplexing properties of all the channels of the tandem AWG filter.

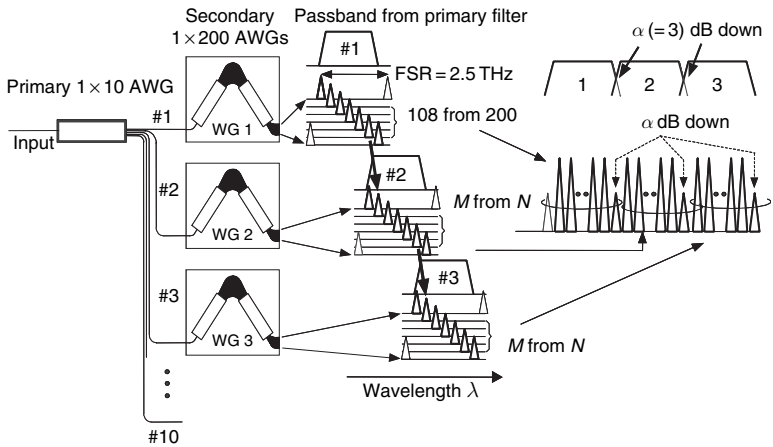

Figure 9.43 Configuration of 10 GHz-spaced 1010-channel tandem AWG.

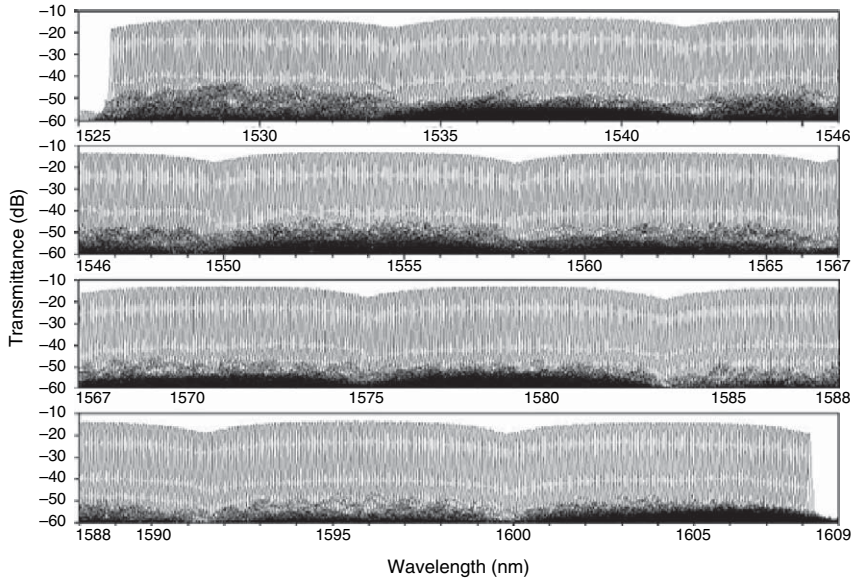

Figure 9.44 Demultiplexing properties of all the channels of the tandem AWG filter.

There are a total of 1010 channels and they are all aligned at 10 GHz intervals with no missing channels in the 1526- to 1608-nm wavelength range. The loss values ranged from 13 to 19 dB. The main origin of the 13 dB loss is the 10-dB intrinsic loss of the primary AWG. This could be reduced by about 9 dB when a 1×10 interference filter is used instead of a flat-top AWG or by using a flat-top AWG design that does not have intrinsic loss. A 4200-channel AWG with 5-GHz channel spacing has also been fabricated by using the tandem configuration [55–57].

Chirped AWGs

Non-technical overview: A bird's chirping is a change in pitch while the bird is uttering a sound. A chirped grating is a change in pitch across the grating. A chirped AWG means that the path-length difference between adjacent arms is not constant.

All the AWGs discussed so far have had a constant path-length difference between adjacent grating waveguides. If we use a variable path-length difference, we create a "chirped" AWG. We will discuss two main types of chirped AWGs. The first is where the arm path length vs arm number has a quadratic component. We will call this "linear chirping." The second is where the path-length difference between adjacent arms oscillates between two values. We will call this "interleave chirping."

Linear Chirping By adding a significant quadratic component to the arm length distribution, and then quantizing it to an integer multiple of a desired wavelength, one can have an imaging focal length in the AWG that changes significantly with wavelength [58, 59]. In other words,

$$L(i) = \text{round}\left\{ m\left[i + \gamma\left(i - \frac{I+1}{2} \right)^2 \right] \right\} \frac{\Delta L}{m} \tag{9.29}$$

where γ is the amount of chirp, m is the operating grating diffraction order, and I is the total number of grating waveguides. "round" means round to the nearest integer. We call this linear chirping. Linear chirping can be used to make one grating order have a higher transmissivity than others. This was used to make a tunable laser consisting of a silica AWG and semiconductor optical amplifier oscillate in a desired grating order [60]. If one wishes to have multiple ports in focus simultaneously in a linearly chirped AWG, one needs to distort the output star coupler. One can tilt the focal line of the star coupler at the output ports, vary the grating port pitch linearly, or a combination of both.

Interleave Chirping An interleave-chirped AWG has interleaved sets of grating arm lengths with different properties. Two main types have been demonstrated. One is the different sets of waveguides have a small difference in their path-length difference and has been used to create flat-top passbands in AWGs [61], as mentioned in Section "Flat Spectral-Response AWGs." This technique necessarily adds insertion loss, however, in accordance with the Flat-Top Filter Construction Theorem. The other is the different sets of waveguides have approximately the same path-length difference, but there is a phase-shift difference between them, and has been used to create a wavelength-selective switch (WSS) [62].

Figure 9.45 shows the waveguide layout for the WSS. It consists of two interleave-chirped AWGs connected by an AWL with thermooptic phase shifters in each arm. The odd-numbered grating waveguides in the interleaver-chirped AWGs have a $\lambda/4$ extra path length as compared with the even-numbered grating waveguides. This causes two images to be generated by the AWG at each wavelength. The AWL is connected so as to pick up these two images plus one extra image from outside the central Brillouin zone. Thus, there are three images per wavelength channel. There are two input waveguides and two output waveguides for the WSS. By controlling the relative phases between the three images for each channel, each channel can be routed independently from either input waveguide to either output waveguide. The three phases help provide an improved extinction ratio. The lower part of Figure 9.45 shows the measured transmissivity for one switching state. Although this WSS has a low insertion loss and is compact, thermal crosstalk between phase shifters in the WSS makes it difficult to control.

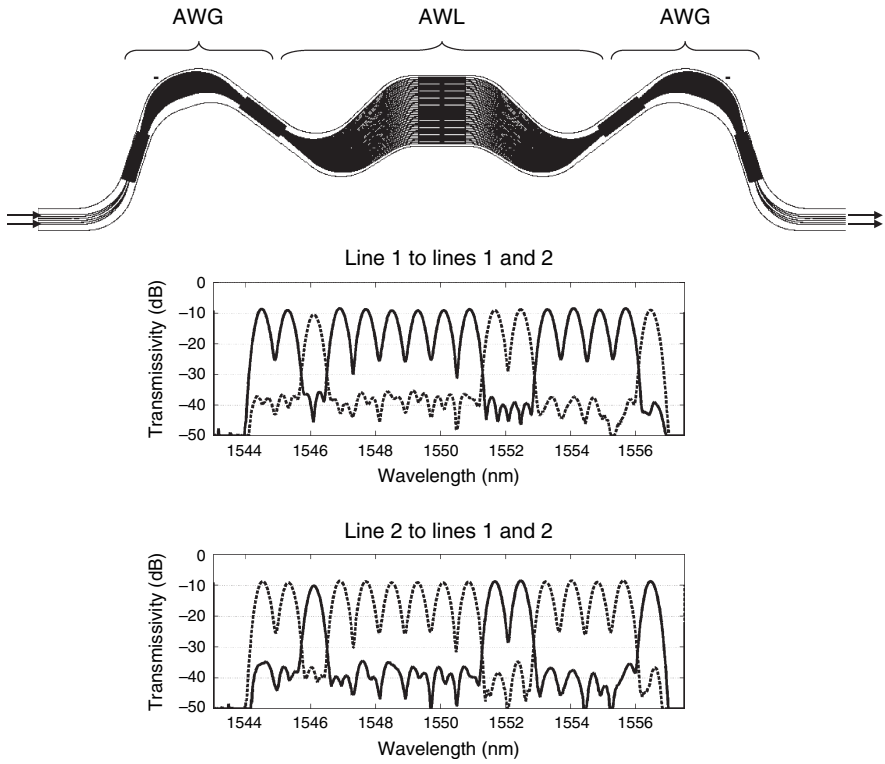

Figure 9.45 WSS made using two interleave-chirped AWGs and an AWL.

9.3.3 Planar Holographic Bragg Reflectors

Non-technical overview: This type of optical device has very little to do with real holograms, which are images where the magnitude and phase of the light is recorded, rather than just the intensity as in conventional photography, allowing for three-dimensional images. The device here is simply a two-dimensional array of weak reflectors. In one-dimension, it is simply a Bragg reflector. The reflections add constructively at various wavelengths and in various directions to create optical filters.

A planar holographic Bragg reflector consists of very fine etched features in part of the core (some of the core must remain in order to maintain vertical confinement) in concentric arcs. These act as two-dimensional Bragg reflectors. High-resolution lithography is required to fabricate such devices. This type of device is not a photonic crystal. By definition, a photonic crystal is made of high index contrast, so that it can exhibit a band gap over a large range of

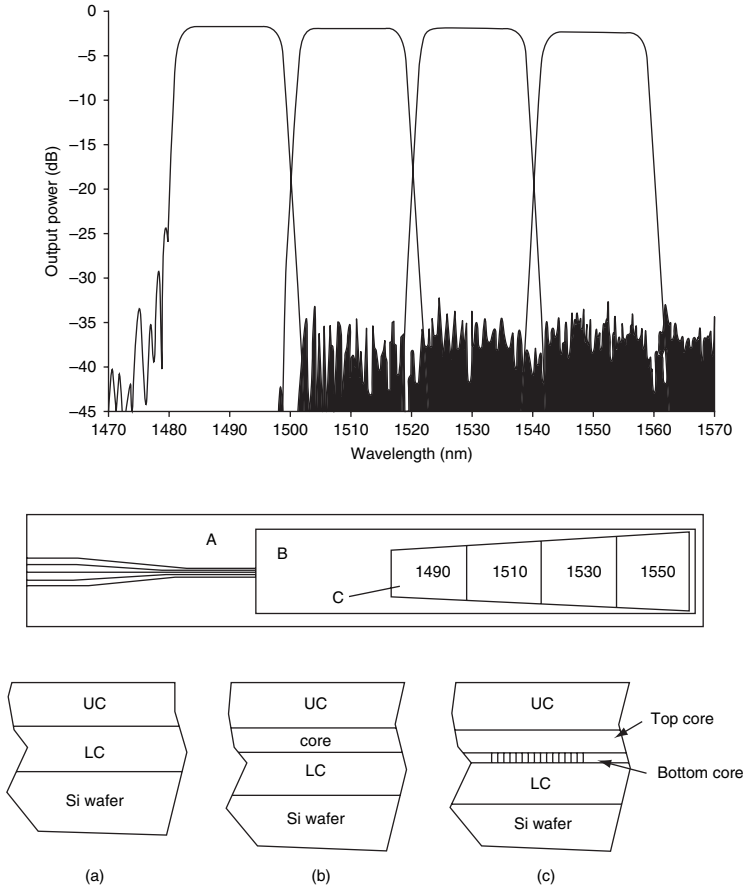

Figure 9.46 4-Channel CWDM multiplexer made using a planar holographic Bragg reflector. The two-dimensional Bragg reflector region is in area C. From Ref. [63].

propagation directions, whereas a planar holographic Bragg reflector is typically made of low index contrast material. An example of 4-channel CWDM multiplexer using this technology is shown in Figure 9.46 [63].

9.4 INTER-SIGNAL CONTROL DEVICES

Non-technical overview: By inter-signal control, we mean control of the overall spectrum of multiple wavelength channels in a WDM system. The devices in this section are dynamic devices that can power-regulate and route wavelength channels in WDM networks.

9.4.1 Reconfigurable Optical Add/Drop Multiplexers

A reconfigurable optical add/drop multiplexer (ROADM) is a device that gives simultaneous access to all wavelength channels in WDM communication systems. The first PLC integrated optic ROADM was fabricated and basic functions of individually routing 16 different wavelength channels with 100-GHz channel spacing were demonstrated in Ref. [64]. The waveguide configuration of the 16-channel optical ROADM is shown in Figure 9.47. It consists of four arrayed-waveguide gratings and 16 double-gate thermooptic switches (TOSWs). Four AWGs are allocated with crossing their slab regions with each other. These AWGs have the same grating parameters; they are the channel spacing of 100 GHz and the free spectral range of 3300 GHz (26.4 nm) in the 1.55-μm region. Equally spaced WDM signals, $\lambda_1, \lambda_2, \ldots, \lambda_{16}$, which are coupled to the main input port (add port) in Figure 9.47 are first demultiplexed by the AWG_1 (AWG_2) and then 16 signals are introduced into the left-hand-side arms (right-hand-side arms) of double-gate TOSWs. The crossing angle of the intersecting waveguides is designed to be larger than 30° so as to make the crosstalk and insertion loss negligible.

Here, the "off" state of a double-gate switch is defined as the switching condition in which a signal from a lower left input port (right input port) goes to an upper right output port (left output port) in Figure 9.47. The "on" state is then defined as the condition in which a signal from a lower left input port (right input

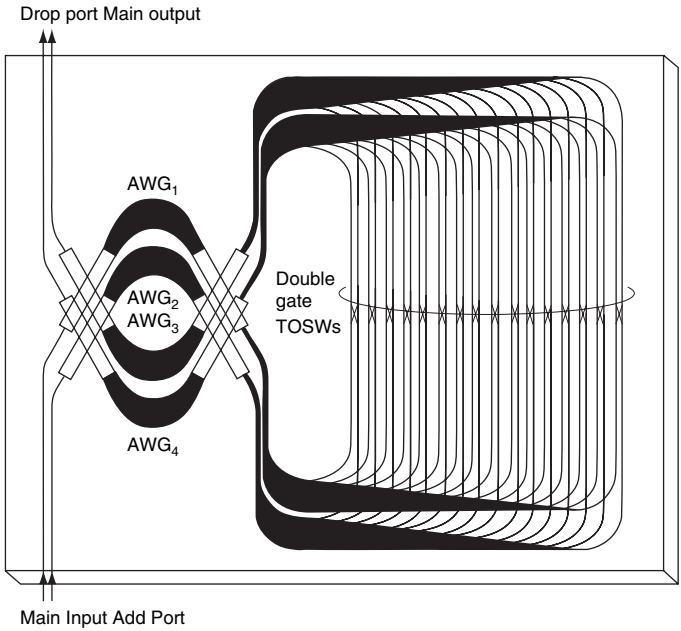

Figure 9.47 Waveguide configuration of 16ch ROADM with double-gate thermo-optic switches (TOSWs).

port) goes to a lower left output port (right output port). When a double-gate switch is "off," the demultiplexed light by AWG_1 (AWG_2) goes to the cross arm and is multiplexed again by AWG_3 (AWG_4). On the other hand, if a double-gate switch is "on" state, the demultiplexed light by AWG_1 (AWG_2) goes to the through arm and is multiplexed by AWG_4 (AWG_3). Therefore, any specific wavelength signal can be extracted from the main output port and led to the drop port by changing the corresponding switch condition. Signals at the same wavelength as that of the dropped component can be added to the main output port when it is coupled into the add port in Figure 9.47.

Figure 9.48 shows light transmission characteristics from main input port to main output port (solid line) and drop port (dotted line) when all TO switches are "off." The on-off crosstalk is smaller than -33 dB with the on-chip losses of $7.8 \sim 10.3$ dB. When TO switches SW_2, SW_4, SW_6, SW_7, SW_9, SW_{12}, SW_{13}, and SW_{15}, for example, are turned to "on" the selected signals λ_2, λ_4, λ_6, λ_7, λ_9, λ_{12}, λ_{13}, and λ_{15} are extracted from main output port (solid line) and led to the drop port (dotted line) as shown in Figure 9.49. The on-off crosstalk is smaller than -30 dB with the on-chip losses of $8 \sim 10$ dB.

Figure 9.50 is a waveguide configuration of an athermal 16-channel ROADM [65]. The silicone-type athermal technique is incorporated in this ROADM. Transmission spectra become essentially insensitive to temperature change, as shown in Figure 9.51.

Although the electric power necessary to drive a double-gate switch is two times larger than the conventional TO switch, the power consumption itself can be reduced from $\sim$1/5 to 1/2 when bridge-suspended phase shifters [66] or a trench/groove structure [67] are utilized. The present ROADM can transport all input

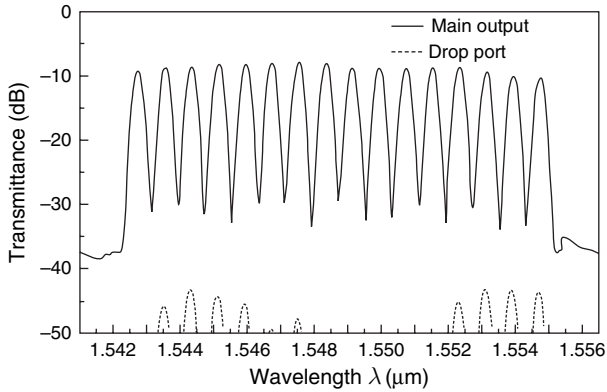

Figure 9.48 Transmission spectra from main input port to main output port (solid line) and drop port (dotted line) when all TO switches are "off."

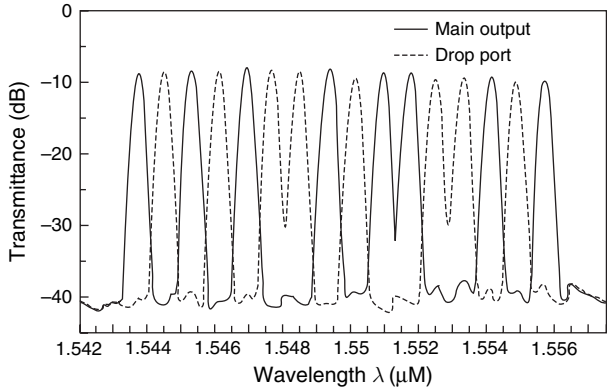

Figure 9.49 Transmission spectra from main input port to main output port and drop port when TO switches SW_2, SW_4, SW_6, SW_7, SW_9, SW_{12}, SW_{13} and SW_{15} are "on."

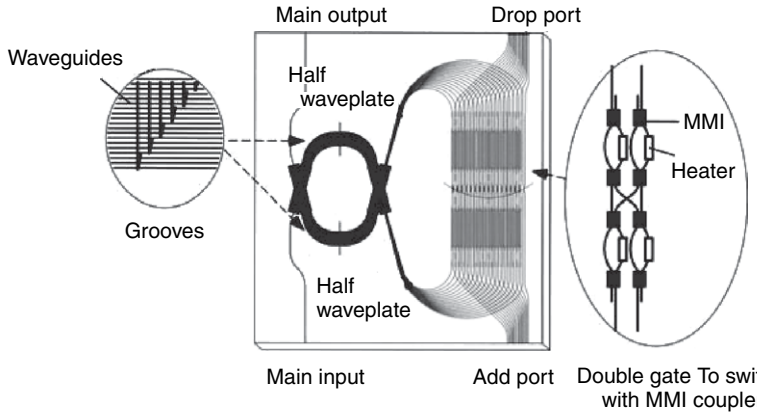

Figure 9.50 Configuration of athermal 16-ch ROADM (this figure may be seen in color on the included CD-ROM).

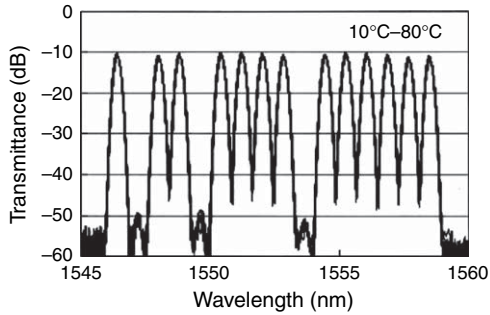

Figure 9.51 Transmission spectra of athermal 16-ch ROADM.

signals to the succeeding stages without inherent power losses. Therefore, these ROADMs are very attractive for all optical WDM-routing systems and allow the network to be transparent to signal formats and bit rates.

9.4.2 Large Channel Count ROADMs

The first demonstrated PLC ROADM was discussed above in Section 9.4.1. This 16-channel demonstration has numerous waveguide crossings, which can require significant wafer real estate because the crossings must occur at a steep angle to mitigate loss and crosstalk. To scale to a very large channel count, one approach is to use a reflective design with a striped mirror facet [68]. One such design had through passbands with two zero-loss maxima by employing two waveguides per channel. One design used perfect spectral sampling across the entire spectrum to achieve no gaps between through channels, shown in Figure 9.52. A difficulty with this design is that after fabrication, one had to manually trim the phases in all the waveguides using electrical hyperheating to phase-align all the spectral components. Another design that is easier to manufacture used perfect spectral sampling only in pairs [69]. In this case, only the phase alignment within each pair needed to be trimmed. However, the full-flat passband between adjacent through channels was lost. Yet another design used an MZI input to create a 64-channel colored ROADM with flat-top passbands (as described in Section "AWG with

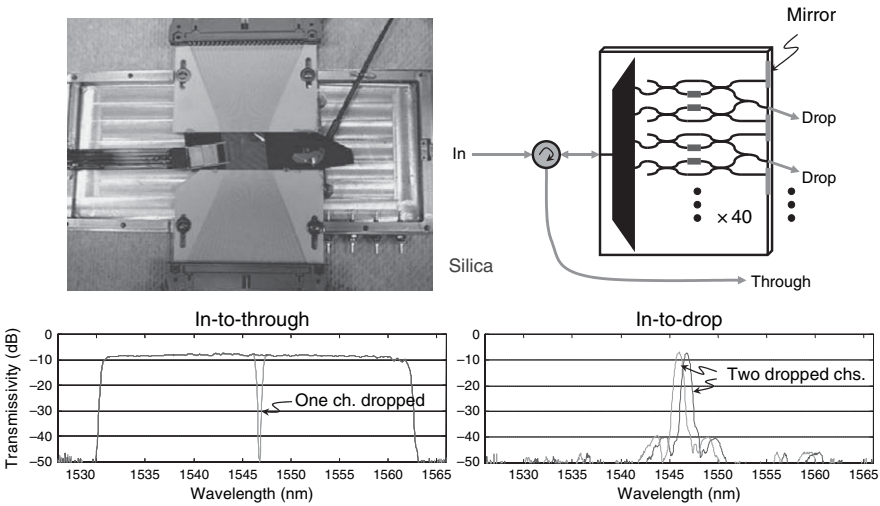

Figure 9.52 40-Channel reflective ROADM using an AWG with perfect spectral sampling. Schematic (upper right), photograph (upper left), measured in-to-through spectra (lower left), and measured in-to-drop spectra (lower right) (this figure may be seen in color on the included CD-ROM).

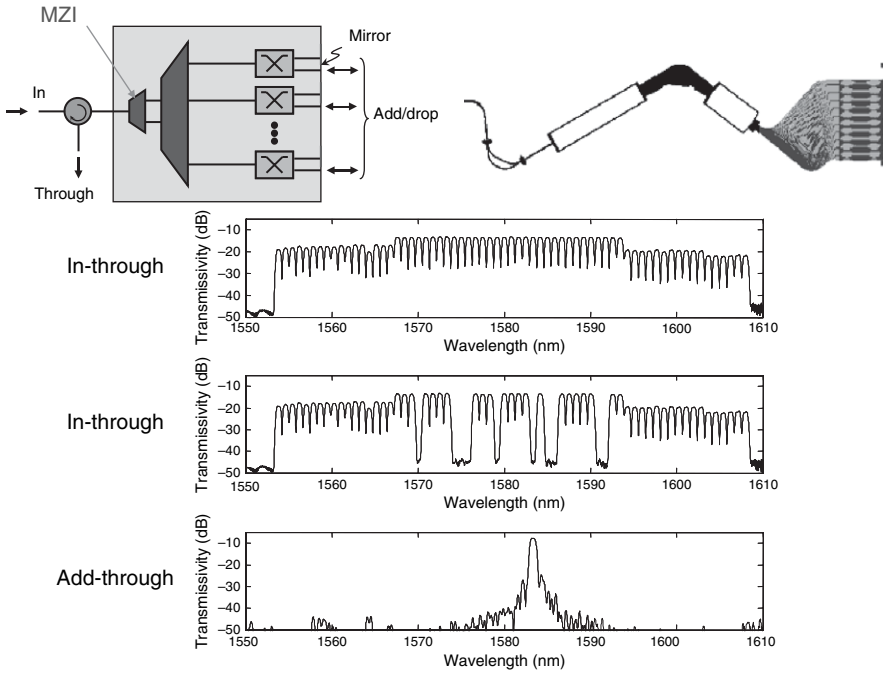

Figure 9.53 64-Channel reflective ROADM using an MZI input to the AWG (this figure may be seen in color on the included CD-ROM).

Two-Arm-Interferometer Input"), shown in Figure 9.53 [70]. In this case, only one phase alignment in the entire device, the MZI to the AWG, needed to be performed.

9.4.3 Wavelength-Selective Switches

A J × K WSS is a device that routes WDM signals from J inputs to K outputs and can be used to make a ROADM. There are many different types. We showed two examples of 2 × 2 WSSs in Sections "Interleave Chirping" and "Reconfigurable Optical Add/Drop Multiplexers." The most common deployed type is a 1 × K WSS. A 1 × K WSS can be used to create a colorless ROADM or an optical mesh node. Another type is a 1 × 1 WSS, which is often called a blocker. It can either block or pass each WDM channel that passes through it. Several PLC blocker demonstrations have been reported [71].

Figure 9.54 shows a waveguide layout of a 1 × 9 WSS [72]. It uses ten 200-GHz-spacing, 8-channel AWGs (1 as a demultiplexer and 9 as multiplexers) and a tree arrangement of 1 × 2 thermooptic switches and a final stage of shutters for improved switching extinction ratio and also to provide a VOA function. It also includes a star coupler with eight VOAs to act as an add-channel combiner.

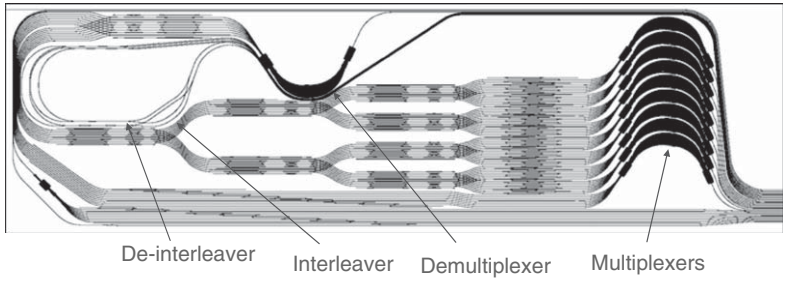

Figure 9.54 8-channel 1×9 WSS (this figure may be seen in color on the included CD-ROM).

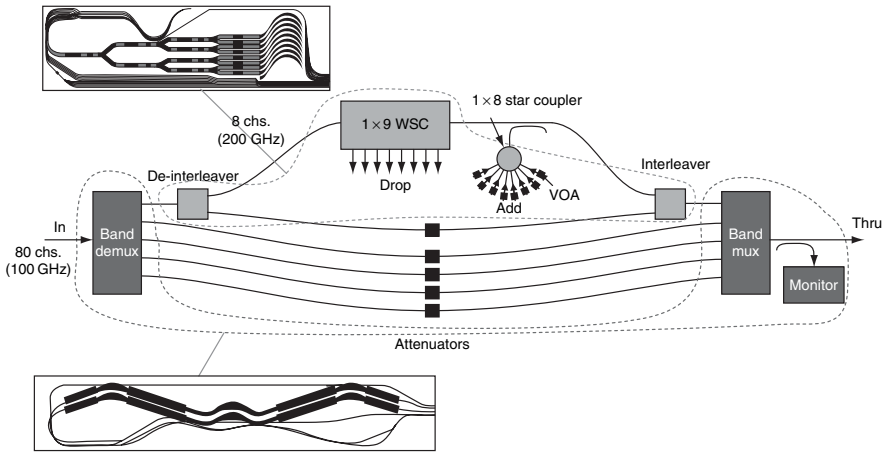

Figure 9.55 Modular 80-channel partially colorless ROADM (this figure may be seen in color on the included CD-ROM).

Furthermore, it includes a de-interleaver to divide an incoming stream of 100-GHz-spaced channels into two streams of 200-GHz-spaced channels and a corresponding interleaver.

This 1×9 WSS PLC, along with a band de/multiplexer PLC, were developed to create a modular 80-channel ROADM, shown in Figure 9.55 [73].

9.5 INTRA-SIGNAL CONTROL DEVICES

Non-technical overview: By intra-signal control, we mean control of the characteristics of the spectrum of a single wavelength channel. The devices in this section are dynamic devices that can modify the waveforms of optical signals, in order to create desired pulse shapes, overcome transmission impairments, etc.

9.5.1 Temporal Pulse Waveform Shapers

Non-technical overview: A temporal pulse waveform shaper is an arbitrary waveform generator (which unfortunately has the same acronym as AWG). It consists of taking a period pulse train, spectrally demultiplexing all the spectral components, controlling the amplitude and phase of each component, and then multiplexing them back together.

The shaping and encoding of optical pulse waveforms are important for a variety of applications in optical communications, optical radar, and picosecond and femtosecond spectroscopy. Control of the pulse temporal profile is achieved by spatially dispersing the optical frequency components, whose amplitude and phase are arbitrarily weighted and multiplexing them again into a single optical beam. Weiner et al. [74] first demonstrated a technique for optical pulse shaping using a grating pair as a dispersive element and masks for amplitude and phase filtering. Because they used a grating pair, the size of the experimental apparatus was of the order of 1 m^2. Also, the weighting functions for the amplitude and phase masks were fixed because they fabricated them by metal deposition and reactive-ion etching of the silica glass.

A schematic configuration of a fully integrated optic dynamic temporal pulse waveform shaper is shown in Figure 9.56 [75]. It consists of an AWG pair for demultiplexing (AWG_1) and multiplexing (AWG_2) the spectral components of mode-locked optical pulses and TOSWs and phase shifters for arbitrarily patterning the spectral components. The channel spacing and total number of channels of

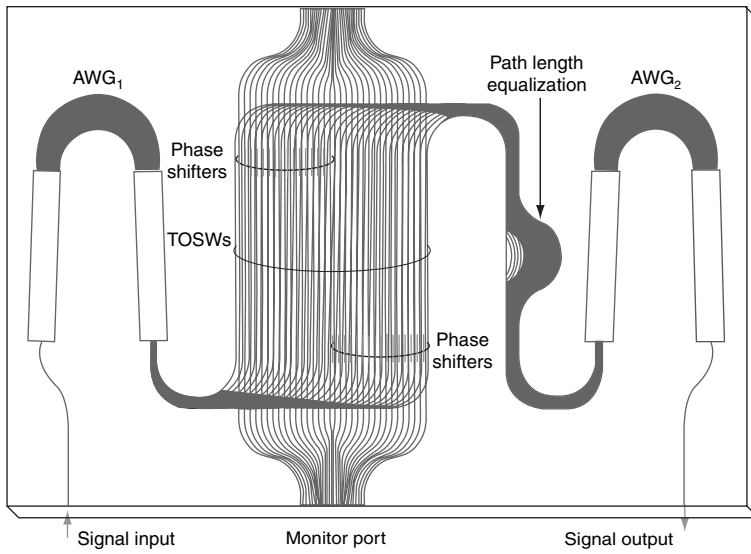

Figure 9.56 Schematic configuration of temporal pulse waveform shaper (this figure may be seen in color on the included CD-ROM).

the AWG are 40 and 80 GHz, respectively, which are centered at $\lambda_0 = 1.55\,\mu$m. About 32 channels among 80 channels of the AWG are used for spectral filtering. An array of 32 TOSWs and phase shifters are allocated between the AWG pair. All the optical path lengths from AWG_1 to AWG_2 are made equal by employing path-length adjustment waveguides. The switching ratio of each TO switch, which can be controlled essentially from 0 to 1, is measured by using the monitor port. Also, the amount of phase shift in each path is determined by comparing the relative phase difference with a reference arm. The fiber-to-fiber insertion loss is 12 dB, and the extinction ratio is ~30 dB. The average electric power for each TO switch is ~300 mW. The minimum controllability of the electric power is 1–2 mW. This enables us to obtain 0.1–0.2 dB amplitude controllability. The average electric power necessary to obtain π phase shift is also about 300 mW. According to this minimum controllability of electric power, the phase-shifter resolution is about $\pi/100$.

The temporal pulse waveform shaper can be utilized in a variety of applications for optical pulse multiplexing, pulse waveform shaping, frequency chirping compensation, and frequency-encoding code division multiplexing (FE-CDM). *N* times optical pulse multiplication can easily be accomplished by filtering the line spectral components of the mode-locked pulse in every *N*th interval.

A square-shaped optical pulse is a particularly useful pulse shape with potential application to nonlinear optical metrology, coherent transient spectroscopy, and future all-optical switching and optical demultiplexing [76, 77]. Figure 9.57 shows

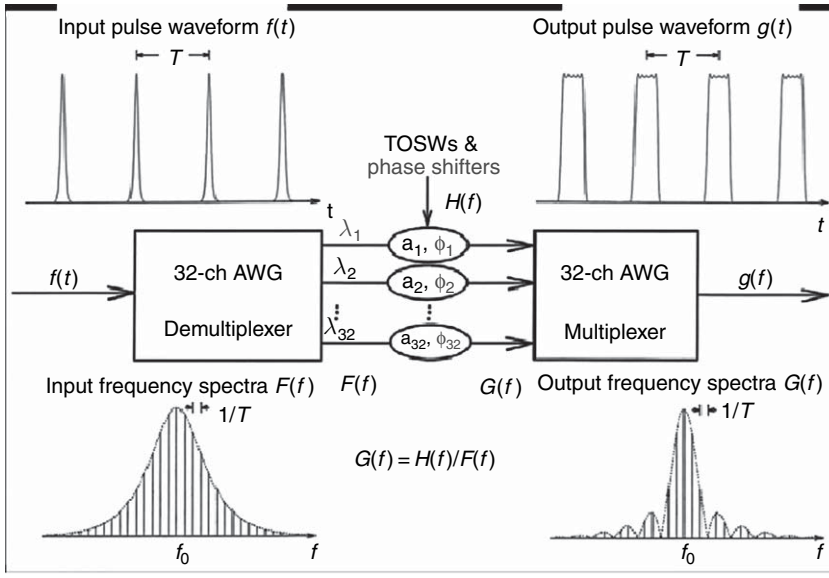

Figure 9.57 Schematic pulse waveforms and frequency spectra in square pulse generation scheme (this figure may be seen in color on the included CD-ROM).

the schematic temporal pulse waveforms and frequency spectra in the square pulse-generation scheme. The frequency spectrum of a mode-locked pulse train with the waveform $f(t) = A \cdot \mathrm{sech}(t/t_0)$ is given by

$$F(f) = \sum_{m=-\infty}^{\infty} A \cdot \sec \mathrm{h}\left[\pi^2 t_0 (f - f_0)\right] \delta\left(f - f_0 - \frac{m}{T}\right), \tag{9.30}$$

where f_0, T, and t_0 denote center frequency, pulse interval, and pulse width (FWHM width $\tau = 2\cosh^{-1}\sqrt{2} \cdot t_0 \cong 1.763 t_0$), respectively. In order to generate square pulses with rise and fall times of $(t_2 - t_1)$, the corresponding sinc-like frequency spectra with the form

$$G(f) = \sum_{m=-\infty}^{\infty} \frac{\sin[\pi(t_2 + t_1)(f - f_0)]}{\pi(t_2 + t_1)(f - f_0)} \cdot \frac{\cos[\pi(t_2 - t_1)(f - f_0)]}{1 - [2(t_2 - t_1)(f - f_0)]^2} \cdot \delta\left(f - f_0 - \frac{m}{T}\right), \tag{9.31}$$

should be synthesized. Then, the amplitude and phase-weighting function $H(f)$ of the pulse shaper for each spectral component is determined by $H(f) = G(f)/F(f)$. Here, we assume $T = 25$ ps, $\tau = 8$ ps, $t_1 = 3.3$ ps, $t_2 = 5.3$ ps, and $f_0 = 1.931$ THz.

Figure 9.58(a) and (b) shows the experimental original spectra and auto-correlated pulse waveforms [78]. The original pulse had an FWHM of $\tau = 0.9$ ps. Figure 9.59(a) and (b) shows synthesized spectra and corresponding cross-correlated pulse waveforms for designed pulse widths of $\tau = 11.9$ ps. Dotted and solid lines show designed and experimental values, respectively. The ripples in the flat-top pulse region are caused by the finite available bandwidth and are estimated to be 0.1 dB compared with the calculated values of 0.2 dB. The rise and fall time (10% to 90%) is 2.9 to

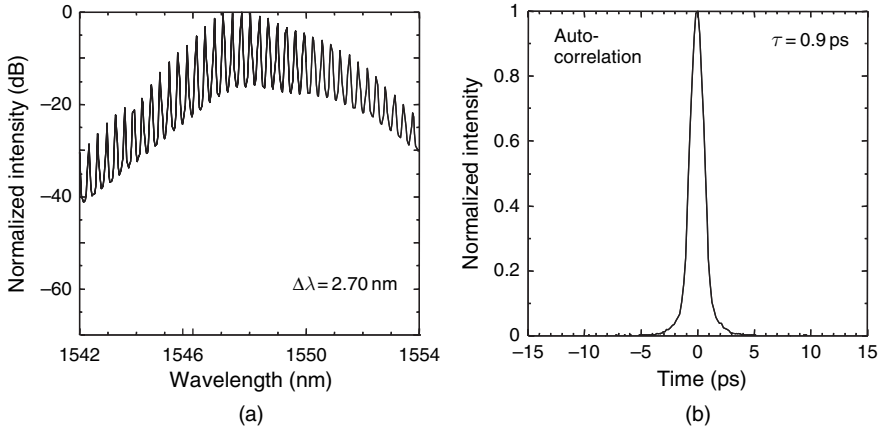

Figure 9.58 (a) Experimental original spectra and (b) auto-correlated pulse waveforms.

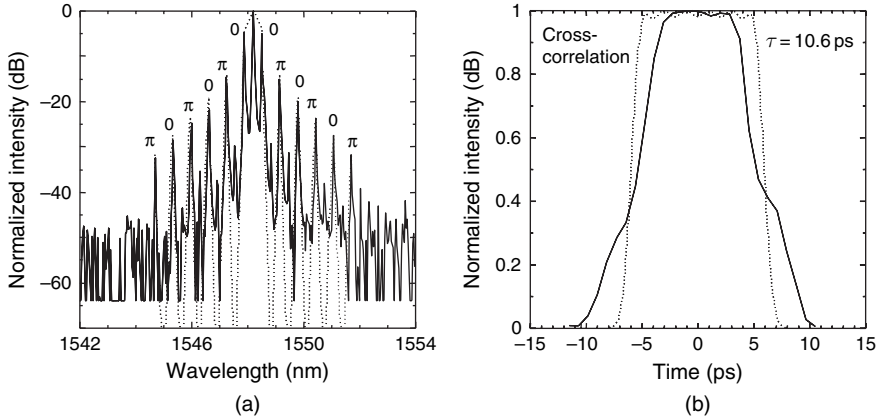

Figure 9.59 (a) Synthesized spectra and (b) corresponding cross-correlated pulse waveforms for designed pulse widths of $\tau = 11.9$ ps.

5.4 ps, while the designed values are both 1.5 ps. The deterioration in the rise and fall time is mainly brought about by phase-setting errors that originated in the thermal crosstalk among the phase shifters used for TO phase adjustment. Phase-setting errors could be reduced by using heat-insulating grooves.

9.5.2 General Optical Equalizers

Non-technical overview: An optical equalizer (at least a linear one) is simply an optical filter that serves to improve a signal that was degraded due to deterministic distortions. By "optical filter," we mean any optical element with some sort of spectral response, in amplitude, phase, or both. It does not have to filter anything, and in fact, it is not an equalizer's job to mitigate noise. A tunable optical dispersion compensator is a type of equalizer, and indeed, the first dispersion compensators were called equalizers.

An equalizer is a device that at least partially restores a signal corrupted by deterministic intersymbol interference (ISI). ISI is the mixing together of different time components in the signal. Example causes of ISI are limited transmitter modulator bandwidth, chromatic dispersion in optical fiber, narrow optical filters, and group delay ripple in optical filters. Equalizers successfully undo only deterministic ISI and not random processes, such as spontaneous emission from amplifiers. Equalizers in the electrical domain are a widely used technology. The electrical technology is called electrical equalization (EEQ). Here, we will focus on optical equalization (OEQ).

The simplest type of equalizer is a tapped delay line. A tapped delay line consists of a series of weighted taps and delays which are re-added to the signal. Adjusting the weights' amplitudes and phases allows one to create a desired

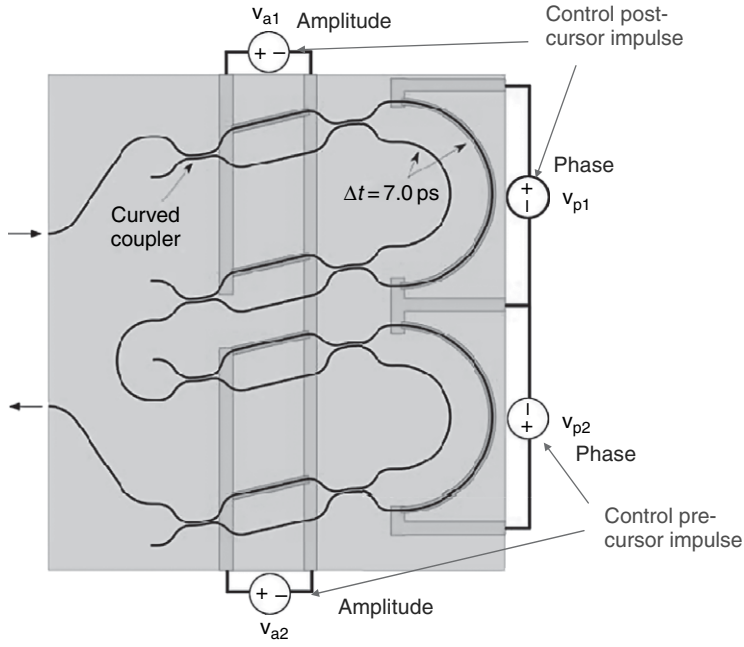

Figure 9.60 Two-tap general OEQ (this figure may be seen in color on the included CD-ROM).

impulse response. Ideally, this impulse response is the inverse of the impulse response that created the ISI, i.e., $h_{EQ}(t) = F^{-1}\{1/F\{h_{ISI}(t)\}\}$. To create a tapped delay line in optics, one can use MZIs. A simple one was demonstrated in [79], and a more complex one, using lattice filters, was demonstrated in [80].

Figure 9.60 shows a simple OEQ—a two-tap OEQ, with one pre-cursor tap and one post-cursor tap. For many ISI impairments, it is found that the best time tap spacing is $\sim$0.7 times the bit period of the digital data signal. Two-tap OEQs have been demonstrated for both 40- and 100-Gb/s signals, correcting modulation bandwidth limitations, extinction ratio limitations, chromatic dispersion, and signal distortion due to narrow optical filtering. It has also been shown to mitigate PMD impairments by signal shaping. By making the OEQ have an FSR that aligns with the WDM channel spacing, a plurality of WDM channels can be equalized simultaneously, provided the ISI on the channels is equal.

Equalization reshapes not only the signal but also the noise. For on-off keyed (OOK) formats, it is better to equalize the signal when the optical signal-to-noise ratio (OSNR) is high, but for PSK formats, initial indications are such that the equalizer is equally effective equalizing when the OSNR is high or low [81].

Such a two-tap OEQ, with a time tap spacing of 7 ps, was used to compensate ISI due to modulator bandwidth limitation and achieve a high-quality 107 Gb/s non-return-to-zero signal [82], as shown in Figure 9.61.

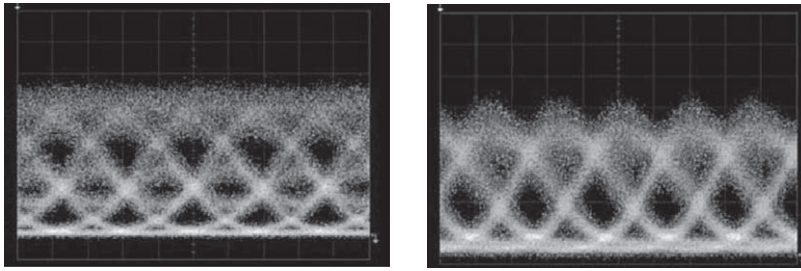

Figure 9.61 107-Gb/s NRZ eye diagram, (a) before and (b) after optical equalization, showing an example of equalization of a bandwidth-limited transmitter (this figure may be seen in color on the included CD-ROM).

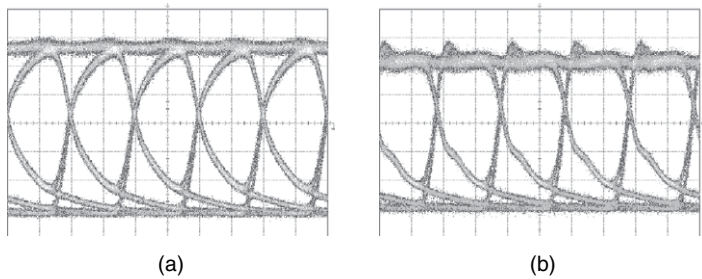

Figure 9.62 Electrical eye diagram of 10-Gb/s signal from a band-limited photodiode before (a) and after (b) optical equalization (this figure may be seen in color on the included CD-ROM).

Although OEQ is highly effective against most transmitter impairments, it is ineffective against most receiver impairments. This is because in order to correct optically for a band-limited direct-detection receiver, one needs to generate a negative optical power, which is impossible. For example, most photodiodes are limited in speed by either a resistor-capacitor (RC) time constant or carrier transport barriers, both of which have an asymmetric impulse response. Thus, a typical band-limited photodiode gives an electrical eye diagram as shown in Figure 9.62(a). An attempt to open the eye using a two-tap OEQ results in the eye diagram shown in Figure 9.62(b) (because the ISI impulse response is asymmetric, the best OEQ setting was also asymmetric). The OEQ can fix the top rail, but is unable to do anything about the bottom rail, because it cannot generate a negative optical power. Instead, one must use an electrical equalizer after the photodiode to fix a band-limited receiver.

A general OEQ optimally needs to have independent adjustment of the amplitude and phase of all its impulses. Some ISI impulse responses are symmetric, whereas others are asymmetric. For example, if a modulator is limited in bandwidth due to an RC effect, the ISI impulse response is asymmetric, whereas if the modulator bandwidth limitation is due to RF transmission line loss, the ISI impulse

response may be symmetric. An even more general OEQ can independently control the impulses for each polarization, and a step toward such an OEQ was shown in Ref. [83].

Although the above OEQs used finite-impulse response (FIR) filters, an OEQ using an infinite-impulse filter was demonstrated using ring resonators in silicon waveguides [84]. Such an OEQ is not a general OEQ, because that OEQ has an asymmetric impulse response, and there is limited control over individual impulses. Such an OEQ is instead a specific equalizer, and the next section covers equalizers specific to optical dispersion compensation. Specific equalizers can compensate much larger distortions than general equalizers, because all the impulses do not need to be individually controlled.

9.5.3 Optical Chromatic Dispersion Compensators

An optical dispersion compensator (ODC) is an optical equalizer optimized to compensate chromatic dispersion. It is often used to compensate the chromatic dispersion encountered in optical fibers; standard single-mode fiber (SSMF) has a dispersion of approximately 17 ps/nm/km in the C-band. If the amount of ODC dispersion is adjustable, the device is called a tunable ODC (TODC). Figure 9.63 shows most of the TODC types that have been demonstrated. They are divided into two main categories: infinite impulse response (IIR) and finite impulse response (FIR) types.

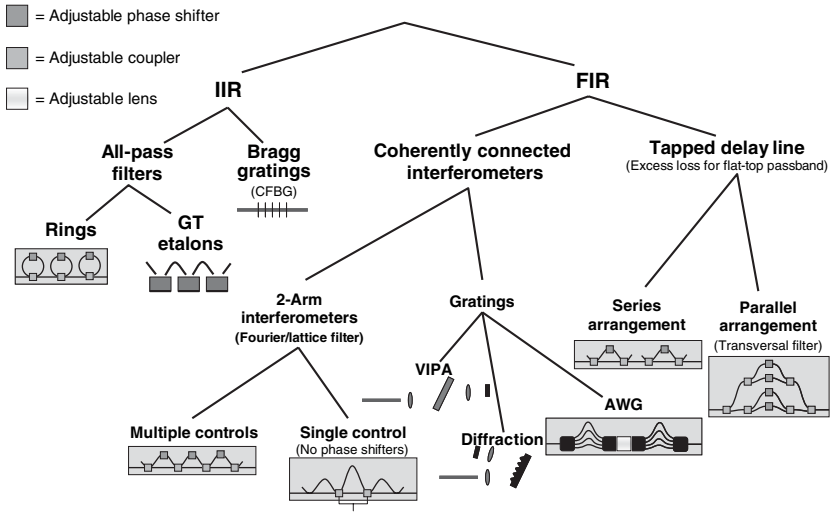

Figure 9.63 Various types of demonstrated TODCs (this figure may be seen in color on the included CD-ROM).

Infinite Impulse Response TODCs

An IIR filter is a filter with an infinite number of impulses and optically is created using resonators. Chromatic dispersion in optical fiber comes from both material effects and waveguiding effects. Both are resonant in nature and thus have an IIR. It is natural to equalize them with another IIR filter.

All-Pass Filters A convenient way to make an IIR dispersion compensator is to use an all-pass filter [85]. An all-pass filter is an IIR filter with constant unity transmissivity but a non-linear phase response as a function of optical frequency.

Ring Resonators: A good example of an all-pass filter is a waveguide coupled to a ring resonator. If the waveguide, coupler, and ring resonator are loss-less, then the light does not experience any loss after passing through the bus waveguide. However, light that has an optical frequency that is resonant in the ring will take a longer time to pass through the bus waveguide. Thus, the group delay will exhibit one peak each ring FSR. By placing several rings in series, all coupled to the same waveguide, and controlling the ring coupling and length, one can create an approximately linear region of group delay, thus generating chromatic dispersion, which can be used to equalize the dispersion encountered in the optical fiber. Although one can imagine other ring configurations to create a TODC, the configuration of Figure 9.64 is the only one demonstrated to date.

A ring resonator coupled to a bus waveguide uses a 2×2 coupler and thus meets the criterion of the Flat-Top Filter Construction Theorem, and, interestingly, generates an infinite number of zero-loss maxima, which is why it is an all-pass filter. Demonstrations of such a TODC are shown in Refs [86, 87].

Gires–Tournois Etalons: A Gires–Tournois etalon consists of a cavity with a 100% reflector at one end and a partial reflector at the other end. If the etalon is illuminated at a slight angle, so that the beam exits at different angle than which it enters and thus can be separated out, then, neglecting beam walk-off, it operates on the same principle as ring resonators. Gires–Tournois etalons have been demonstrated only in bulk material to date (Figure 9.65).

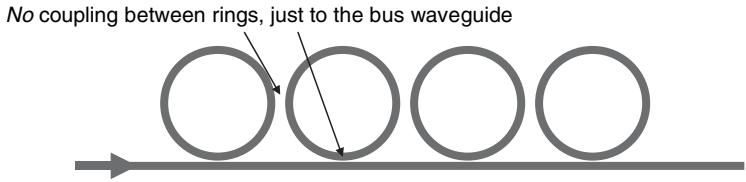

Figure 9.64 TODC using ring resonators in series. Each ring resonator path length is tuned, and usually the coupling to the waveguide bus is also tuned (this figure may be seen in color on the included CD-ROM).

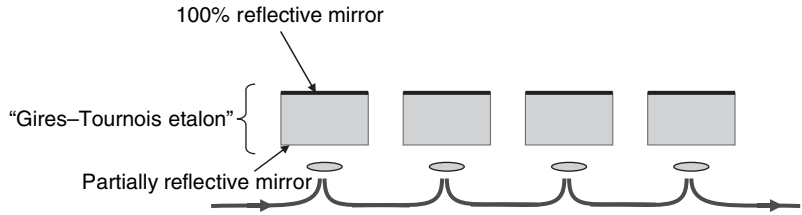

Figure 9.65 TODC using Gire–Tournois etalons (this figure may be seen in color on the included CD-ROM).

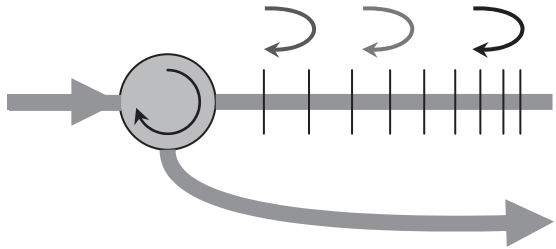

Figure 9.66 Chirped Bragg grating TODC (this figure may be seen in color on the included CD-ROM).

Bragg Gratings Bragg gratings consist of many reflectors in series. Wavelengths that match twice the spacing between reflectors divided by an integer are reflected back. If the Bragg grating has a constantly varying period, i.e., it is linearly chirped, then different wavelengths reflect at different points in the grating, creating chromatic dispersion (Figure 9.66). The dispersion is usually tuned by heating the grating non-uniformly [88]. Bragg gratings are most commonly made in optical fibers, but they have also been demonstrated in silica [89], polymer [90], and InP PLCs.

Finite Impulse Response TODCs

One can also implement dispersion compensation using an FIR filter [91]. An all-pass FIR filter is impossible, so the filter must be designed to have both a linear group delay and a constant transmissivity over the bandwidth of interest. Optically, FIR filters are constructed out of feed-forward interferometers, e.g., MZIs and AWGs.

Tapped Delay Lines We saw an example of an optical tapped delay line in the general OEQ section. Tapped delay line equalizers are commonly used in RF electronics.

Serial Arrangement: A simple tapped delay line filter can be constructed from a serial arrangement of single-mode connected MZIs, as we saw in the general

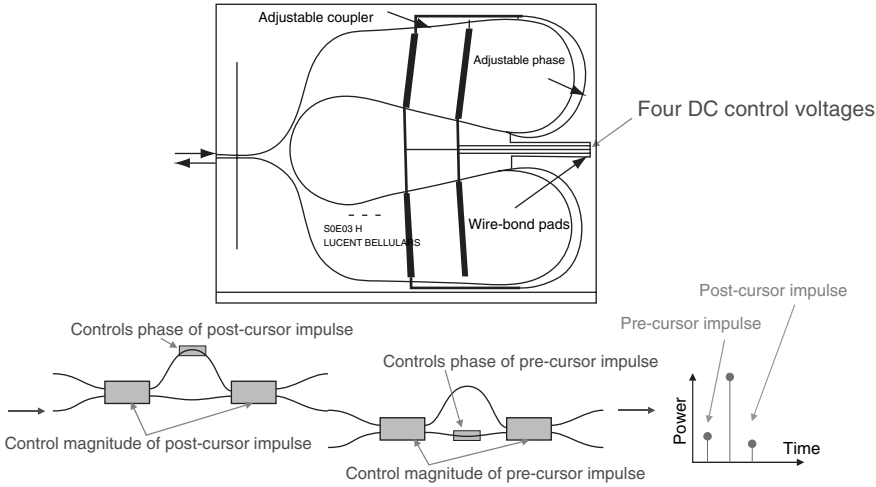

Figure 9.67 Two-tap optical equalizer using a serial arrangement of MZIs (this figure may be seen in color on the included CD-ROM).

OEQ section. Figure 9.67 shows more details of this OEQ. This design has only 1×2 and 2×1 couplers, and thus, according to the Flat-Top Filter Construction Theorem, it has intrinsic loss when used as a TODC.

Parallel Arrangement: Another way to construct a tapped delay line is to use a parallel arrangement of waveguides of different lengths and is called a transversal filter. An example in silica is shown in Figure 9.68 [92], and an example in InP is shown in Figure 9.69 [93]. Again, because transversal filters contain only $1 \times N$ or $N \times 1$ couplers, they have intrinsic loss when used as TODCs. The intrinsic loss

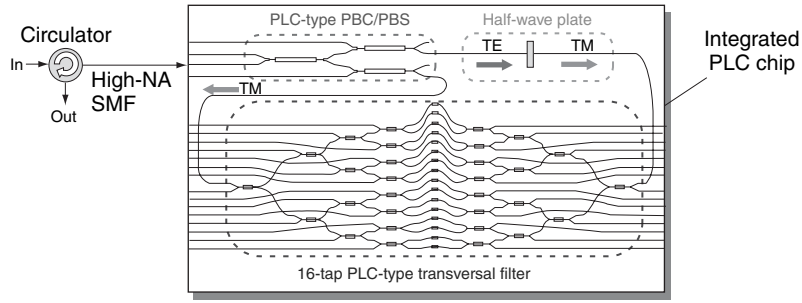

Figure 9.68 TODC using a transversal filter in silica waveguides. The left and right regions contain adjustable couplers, and the center region contains adjustable phase shifters. From H. Kawashima of Ref. [92] (this figure may be seen in color on the included CD-ROM).

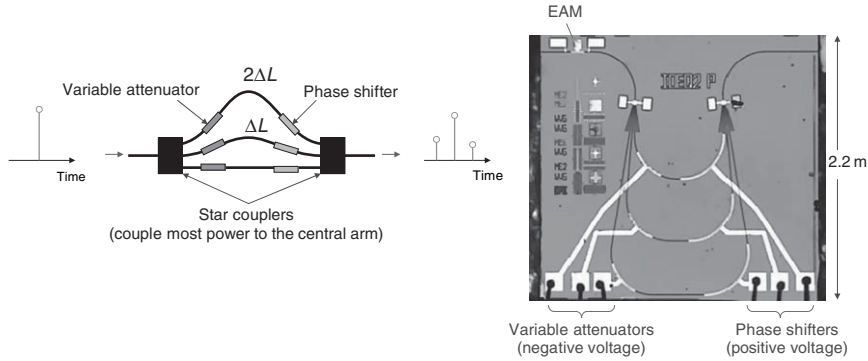

Figure 9.69 TODC using a transversal filter in InP waveguides. This TODC is integrated with an electroabsorption modulator to create a transmitter with integrated dispersion compensation. At left is the concept and at right is a photograph of the chip (this figure may be seen in color on the included CD-ROM).

increases the larger the desired TODC figure of merit (FOM) (defined later in this section).

Coherently Connected Interferometers The previous FIR-based TODCs had only one mode in connections between interferometers. By coherently connected inteferometers, we mean that there are multiple modes (i.e., multiple single-mode waveguides) in connections between interferometers. In other words, there are effective $N \times M$ couplers where N and $M > 1$. This is for the purpose making low intrinsic loss TODCs, according to The Flat-Top Filter Construction Theorem.

Two-Arm Interferometers

Multiple Controls: Figure 9.70 shows a TODC using a series arrangement of 2×2 couplers. Such an arrangement can construct any desired impulse response with N impulses with an arbitrary number of zero-loss maxima per FSR, thus theoretically allowing for an ideal TODC, provided there are at least $N-1$ length-imbalanced MZI stages. To tune the dispersion, all the couplers and all the phases in each MZI arm must be adjusted. Each control affects all the impulses, so the control is complicated.

Single Control: The previous section showed a TODC design constructed from 2×2 couplers with many independent controls. With certain arrangements, one can eliminate the phase controls in the MZI arms and control all the 2×2 couplers with a single control signal.

Figure 9.71 shows such a 3-stage TODC. In this example, the bandwidth was chosen very narrow so as to achieve a large dispersion range. Because of the narrow bandwidth, a filter was integrated with the TODC for having the TODC track the signal wavelength. A feedback loop adjusts the TODC temperature to keep it centered on the signal wavelength. The TODC FSR is chosen quite small so that the temperature change required to lock onto any wavelength is at most ±8°C [94].

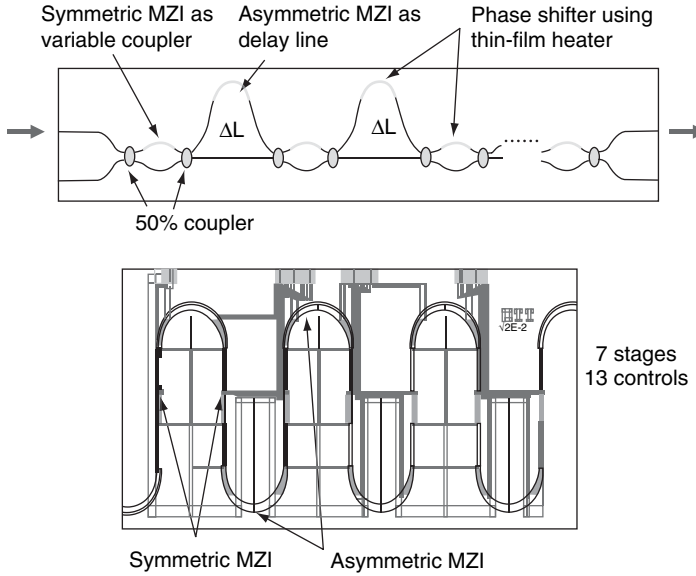

Figure 9.70 TODC using coherently coupled MZIs (this figure may be seen in color on the included CD-ROM).

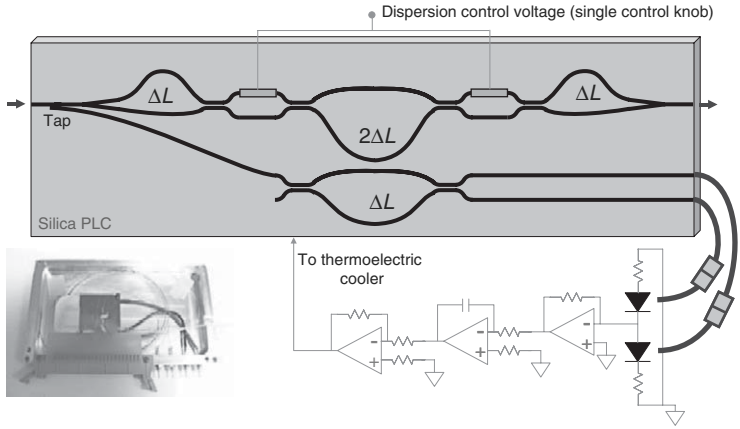

Figure 9.71 3-Stage, 2-arm TODC with a single control for tuning the dispersion. It includes an integrated wavelength-locking monitor (this figure may be seen in color on the included CD-ROM).

A 4-stage design with a single control is shown in Figure 9.72. A 4-stage design has a larger TODC FOM than a 3-stage design. An implementation in silica is shown in Figure 9.73 with an FSR of 100 GHz, which is suitable for 40-Gb/s applications [95]. Results from a 33.3-GHz FSR version are shown in Figure 9.74, which is suitable for 10 Gb/s applications.

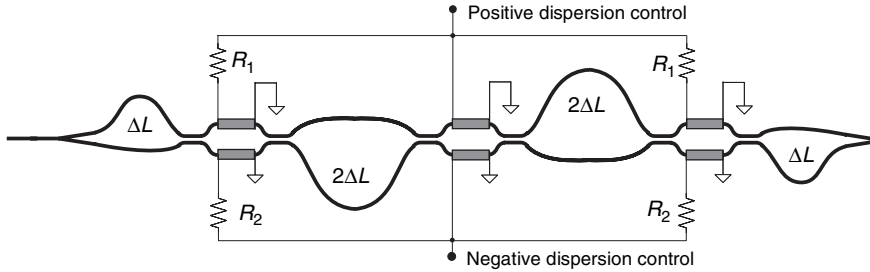

Figure 9.72 4-Stage, 2-arm TODC with a single control for tuning the dispersion (this figure may be seen in color on the included CD-ROM).

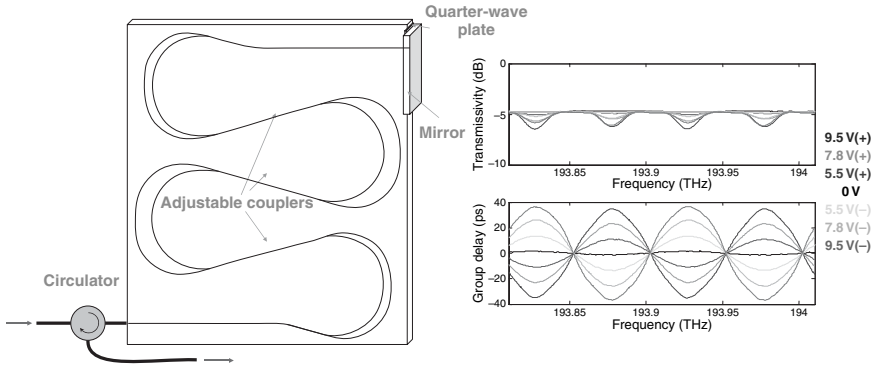

Figure 9.73 4-Stage version realized in a silica PLC. FSR = 100 GHz (this figure may be seen in color on the included CD-ROM).

Gratings: Another way to construct a TODC is to use a diffraction grating, such as a ruled grating, a virtually imaged phased array (VIPA), or an AWG. The basic concept is to spread the spectrum of the signal over an element than can provide a controllable parabolic phase profile (dispersion means a linear group delay which means a parabolic phase vs frequency) and then recombine the spectrum.

Virtually Imaged Phased Array: The VIPA (Figure 9.75) [96] acts like an echelle diffraction grating with extremely high dispersion constructed using a glass or silicon plate with a 100% reflection coating on one side and a partial reflection coating on the other. The plate is tilted such that multiple reflections in the plate create multiple images.

Diffraction Grating: A TODC using a diffraction grating and thermally deformable mirror was demonstrated in Ref. [97]. It used four passes on the grating to achieve a wide passband with low loss at high dispersion settings. No PLC diffraction grating-based TODCs have been reported, to our knowledge.

Arrayed Waveguide Grating: This TODC design consists of two AWGs connected at their second star coupler outer boundaries (where output waveguides would normally be connected). The frequency response measured from input to

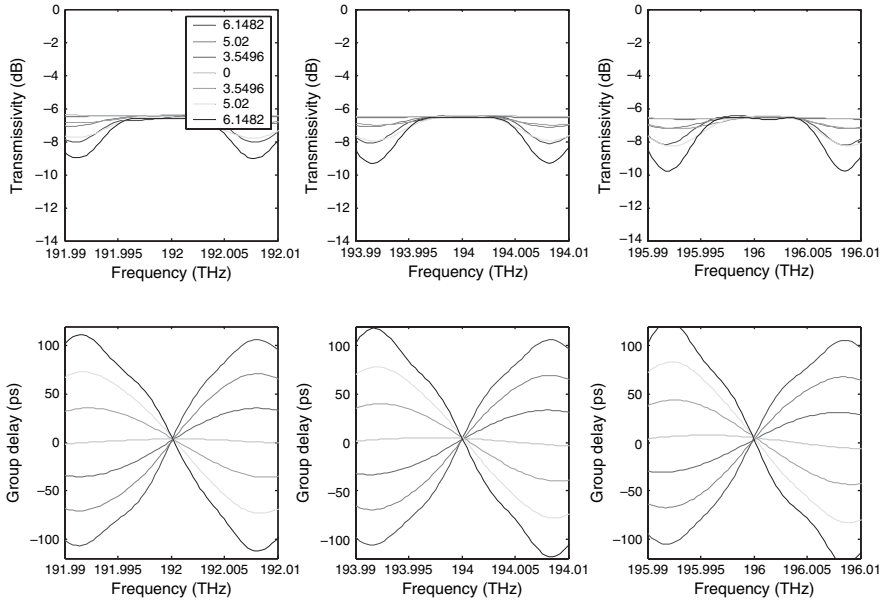

Figure 9.74 4-Stage version in silica PLC with an FSR of 33.3 GHz. The legend shows the voltage setting (this figure may be seen in color on the included CD-ROM).

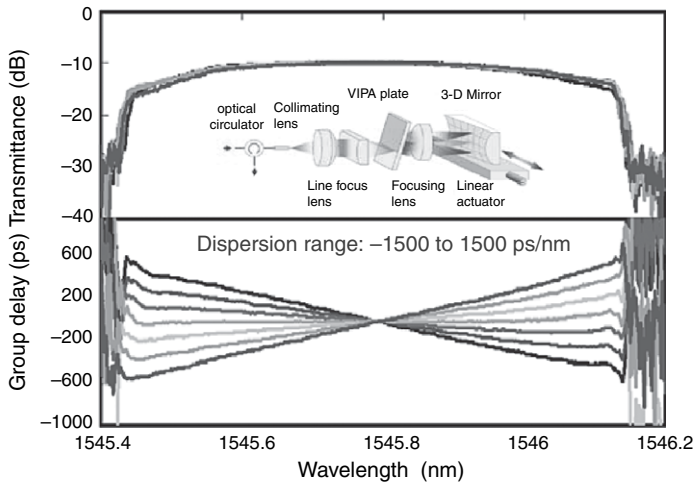

Figure 9.75 TODC using a VIPA. From Ref. [96] (this figure may be seen in color on the included CD-ROM).

output has a Gaussian-shaped passband with a constant negative chromatic dispersion, the dispersion given by

$$D_0 = -\frac{2Rf}{n(a\Delta f)^2}, \tag{9.32}$$

where R is the star coupler radius, n is the refractive index in the slab, a is the grating waveguide pitch at the star coupler, f is the optical frequency (not focal length, as it was used for earlier), and Δf is the AWG FSR. It is usually best to make Δf equal to the WDM channel spacing. Because this device contains an $N \times N$ coupler, it can act as a TODC with low intrinsic loss.

To understand why the device has a negative dispersion, consider the lower part of Figure 9.76. The center lines of the Gaussian beams for two different wavelengths within an FSR are shown. From the left-hand AWG, the wavelengths are focused onto the middle of the double star coupler. Wavelengths longer than the channel center wavelength are imaged below, shorter wavelengths above. After passing the focal line, these beams continue in a straight line, and when they reach the grating arms of the second AWG they are no longer centered. Because the effective path length through an AWG is equal to the average of the path lengths weighted by the power in each path, longer wavelengths end up traveling a shorter path than shorter wavelengths. This is negative dispersion. Note that the off-center beams end up coupling to the output waveguide with a reduced efficiency, and thus, the net passband has a rounded, single-maxima shape.

To tune the dispersion amount, one needs a lensing action as shown at the lower right of Figure 9.76. For example, if a lens with a focal length equal to $R/2$ is placed in the double star center, all the beams are recentered on the grating arms of the second AWG, and the device exhibits zero dispersion. In such a case, the passband is ideally perfect flat, having numerous zero-loss maxima.

One way to create the adjustable lens is to use thermooptics. Because all angles are much less than 1 rad, a lens is just a quadratic index distribution. One way to

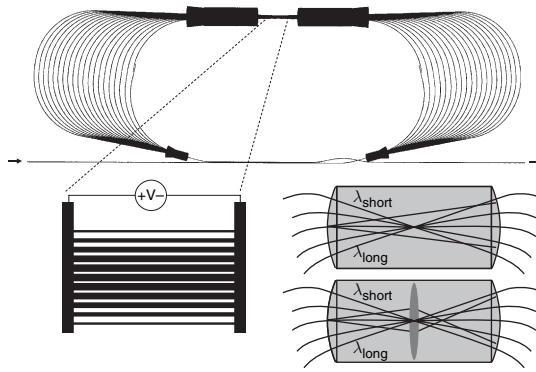

Figure 9.76 AWG-based TODC using a silica thermooptic lens.

create a quadratic index distribution is to drive an array of closely spaced heaters in parallel with a quadratic variation in width. Figure 9.76 shows such a device [98].

However, the electrical power consumption of such a lens when using silica on a silicon substrate can be quite high. In the case above, the power consumption was ~7 W to tune the entire range.

One way to reduce the power consumption is to cut the design in half and make it reflective. This cuts the power consumption in half. To further reduce it, one can use either a deformable mirror [99] or a polymer thermooptic lens, as shown in Figures 9.77 and 9.78 [100]. Polymer gives a large power reduction because the magnitude of its index change with temperature is ~30 times that of silica, and the thermal conductivity of polymer is ~8 times less than that of silica.

Figure of Merit

Let us define an FOM for a TODC, which is usable bandwidth, B (in frequency), squared multiplied by the dispersion adjustment range, ΔD. This FOM is nondimensional, and signal bandwidth squared multiplied by dispersion is an approximate number of bit slots that each bit is spread across by the dispersion. This FOM describes the complexity of the TODC. For example, it is linearly related to the number of ring resonators, the number of MZI stages, or the number of AWG arms in the TODC.

$$\text{TODC FOM} = B^2 \Delta D \frac{\lambda_0^2}{c_0} \tag{9.33}$$

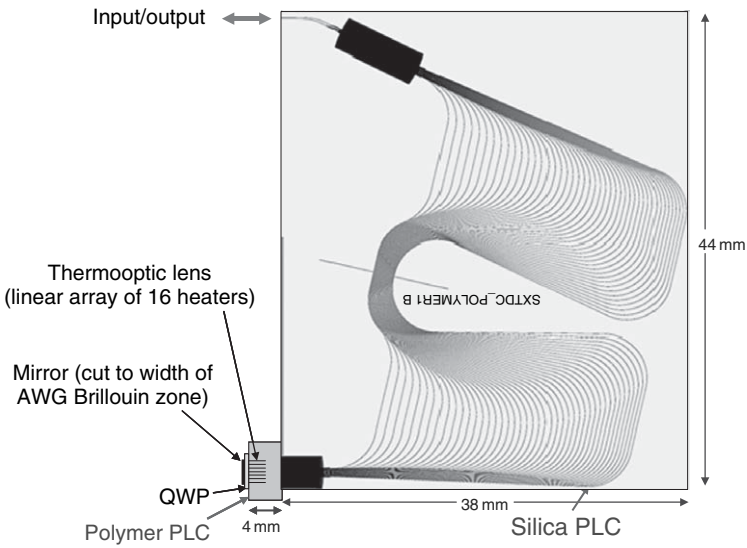

Figure 9.77 AWG-based TODC using a polymer thermooptic lens, in a reflective configuration (this figure may be seen in color on the included CD-ROM).

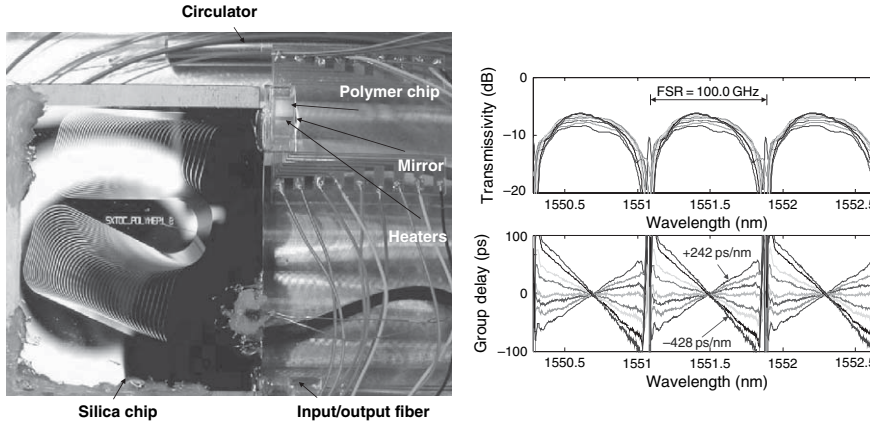

Figure 9.78 Photograph and measured response of AWG-based TODC using a polymer thermo-optic lens (this figure may be seen in color on the included CD-ROM).

Table 9.1
Figure of merit for various demonstrated TODCs.

Type	Reference	ΔD (ps/nm)	B (GHz)	FOM
VIPA	[96]	3000	68	111
CFBG	[101]	800	80	41
AWG*	[82]	1300	39	16
		560	57	15
Etalon	[102]	3400	18	9
Ring*	[87]	3000	19	9
MZI*	[95]	4200	14	7
		420	45	7
Transversal filter*	[92]	200	60	6
Ring*	[86]	900	25	5
MZI*	[91]	300	40	4

* = PLC TODC

Table 9.1 shows approximate FOMs of some currently demonstrated TODCs.

There is actually another FOM for dispersion compensators, but it applies only to dispersion compensating fiber [103]:

$$\text{DCF FOM} = D/L, \tag{9.34}$$

where D is the dispersion and L is the loss. A typical DCF FOM is ~300 ps/(nm-dB). However, the DCF FOM does not apply well to PLC TODCs, because one can easily devise a PLC TODC with arbitrarily large dispersion, but arbitrarily small bandwidth, without significantly affecting the insertion loss and thus even the simplest PLC TODC could exhibit an arbitrarily large DCF FOM.

9.6 CONCLUSION

This chapter gave an overview of many PLC devices that have been demonstrated. We regret that there are many more demonstrated PLC devices that we did not have room to include. We concentrated mostly on silica-based PLCs, but did present some SiON, polymer, and InP PLCs. Si PLCs are currently being vigorously investigated and hold the promise of integration with low-cost electronics. Also, InP PLC research is experiencing a resurgence, because of increasing total data rates. A 10-channel $\times$ 10-Gb/s InP PLC transmitter and InP PLC receiver are now being widely sold commercially [104], and InP PLCs that can produce multilevel formats are currently of great interest.

We focused exclusively on PLCs for fiber-optic communications; and telecommunications is where PLCs were born, and nearly all the significant PLC applications are. However, we believe that for PLC research and development to advance significantly, PLCs must find applications in other areas. There have been small niche non-telecom applications for PLCs, such as fiber-optic gyroscopes; but these are not large enough to have a significant effect on PLC development. Some possible significant alternative PLC applications include radio-frequency (RF) signal processing, biophotonics, displays, and beam steerers/scanners.

It is important to realize that the PLC device with the largest deployed volume today is a simple $1 \times N$ splitter for fiber-to-the-home networks. A key question for PLCs is will photonic circuits more complex than a simple splitter succeed in the *mass market*, like electronic circuits have.

REFERENCES

[1] S. Sohma, T. Goh, H. Okazaki et al., "Low switching power silica-based super high delta thermo-optic switch with heat insulating grooves," *Electron. Lett.*, 38, 127–128, 2002.

[2] B. E. Little, S. T. Chu, P. P. Absil et al., "Very high-order microring resonator filters for WDM applications," *IEEE Photon. Technol. Lett.*, 16, 2263–2265, October 2004.

[3] W. Burns and A. F. Milton, "Mode conversion in planar-dielectric separating waveguides," *IEEE J. Quantum Electron.*, QE-11(1), 32–39, January 1975.

[4] H. Ishikawa, "Fully adiabatic design of waveguide branches," *J. Lightw. Technol.*, 25, 1832–1840, July 2007.

[5] K. Jinguji, N. Takato, A. Sugita, and M. Kawachi, "Mach-Zehnder interferometer type optical waveguide coupler with wavelength-flattened coupling ratio," *Electron. Lett.*, 26, 1326–1327, August 16, 1990.

[6] C. R. Doerr, L. W. Stulz, D. S. Levy et al., "Cross-Connect-Type Wavelength Add-Drop Node with Integrated Band Muxes, Interleavers, and Monitor," in Proc. *OFC* Conference Digest, postdeadline paper PD33, 2003.

[7] M. Oguma, T. Kitoh, Y. Inoue et al., "Compactly Folded Waveguide-Type Interleave Filter With Stabilized Couplers," in Proc. *OFC* Conference Digest, paper TuK3, 2002, pp. 70–72.

[8] C. R. Doerr, M. Cappuzzo, E. Chen et al., "Bending of a planar lightwave circuit 2×2 coupler to desensitize it to wavelength, polarization, and fabrication changes," *IEEE Photon. Technol. Lett.*, 17, 1211–1213, June 2005.

[9] R. Narevich, G. Heise, E. Narevicius et al., "Novel Wide-Band Low-PDL Integrated Variable Optical Attenuator in Silica-on-Silicon," in Proc. *OFC*, paper OthV6, 2005.
[10] K. Takada and S. Mitachi, "Polarization crosstalk dependence on length in silica-based waveguides measured by using optical low coherence interference," *J. Lightw. Technol.*, 16, 1413–1422, August 1998.
[11] M. A. Webster, R. M. Pafchek, A. Mitchell, and T. L. Koch, "Width dependence of inherent TM-mode lateral leakage loss in silicon-on-insulator ridge waveguides," *IEEE Photon. Technol. Lett.*, 19, 429–431, March 2007.
[12] C. R. Doerr, M. A. Cappuzzo, E. Y. Chen et al., "Polarization-insensitive planar lightwave circuit dual-rate Mach-Zehnder delay-interferometer," *IEEE Photon. Technol. Lett.*, 18, 1708–1710, August 2006.
[13] M. K. Smit, "New focusing and dispersive planar component based on an optical phased array," *Electron. Lett.*, 24, 385–386, 1988.
[14] H. Takahashi, S. Suzuki, K. Kato, and I. Nishi, "Arrayed-waveguide grating for wavelength division multi/demultiplexer with nanometer resolution," *Electron. Lett.*, 26, 87–88, 1990.
[15] C. Dragone, C. A. Edwards, and R. C. Kistler, "Integrated optics N × N multiplexer on silicon," *IEEE Photon. Tech. Lett.*, 3, 896–899, 1991.
[16] M. K. Smit and C. Van Dam, "PHASAR-based WDM-devices: Principles, design, and applications," *IEEE J. Sel. Top. Quantum Electron.*, 2, 236–250, June 1996.
[17] K. Okamoto, *Fundamentals of Optical Waveguides* (2nd edn), Academic Press, 2006, Chapter 9.
[18] Y. P. Li and C. H. Henry, "Silicon optical bench waveguide technology," *in Optical Fiber Telecommunications IIIB*, New York, Academic Press, 1997, Chapter 8.
[19] P. Munoz, D. Pastor, and J. Capmany, "Modeling and design of arrayed waveguide gratings," *J. Lightw. Technol.*, 20, 661–674, April 2002.
[20] K. Okamoto, K. Moriwaki, and S. Suzuki, "Fabrication of 64 × 64 arrayed-waveguide grating multiplexer on silicon," *Electron. Lett.*, 31, 184–185, 1995.
[21] K. Okamoto, K. Syuto, H. Takahashi, and Y. Ohmori, "Fabrication of 128-channel arrayed-waveguide grating multiplexer with a 25-GHz channel spacing," *Electron. Lett.*, 32, 1474–1476, 1996.
[22] Y. Hida, Y. Hibino, T. Kitoh et al., "400-channel arrayed-waveguide grating with 25 GHz spacing using 1.5%-Δ waveguides on 6-inch Si wafer," *Electron. Lett.*, 37, 576–577, 2001.
[23] K. Okamoto, "AWG Technologies: Design and their Applications," in Proc. *OFC 2002*, SC113, Baltimore CA, 2002.
[24] K. Okamoto and H. Yamada, "Arrayed-waveguide grating multiplexer with flat spectral response," *Opt. Lett.*, 20, 43–45, 1995.
[25] K. Okamoto and A. Sugita, "Flat spectral response arrayed-waveguide grating multiplexer with parabolic waveguide horns," *Electron. Lett.*, 32, 1661–1662, 1996.
[26] M. R. Amersfoort, J. B. D. Soole, H. P. LeBlanc et al., "Passband broadening of integrated arrayed waveguide filters using multimode interference couplers," *Electron. Lett.*, 32, 449–451, 1996.
[27] D. Trouchet, A. Beguin, H. Boek et al., "Passband Flattening of PHASAR WDM Using Input and Output Star Couplers Designed with Two Focal Points," in Proc. *OFC '97*, ThM7, Dallas, Texas, 1997.
[28] G. H. B. Thompson, R. Epworth, C. Rogers et al., "An Original Low-Loss and Pass-Band Flattened SiO_2 on Si Planar Wavelength Demultiplexer," in Proc. *OFC '98*, TuN1, San Jose, CA, 1998.
[29] C. R. Doerr, L. W. Stulz, and R. Pafchek, "Compact and low-loss integrated box-like passband multiplexer," *IEEE Photon. Technol. Lett.*, 15, 918–920, 2003.
[30] W. K. Burns, A. F. Milton, and A. B. Lee, "Optical waveguide parabolic coupling horns," *Appl. Phys. Lett.*, 30, 28–30, 1977.
[31] T. Kitoh, Y. Inoue, M. Itoh, and Y. Hibino, "Low chromatic-dispersion flat-top arrayed waveguide grating filter," *Electron. Lett.*, 39, 1116–1118, 2003.

[32] T. Chiba, H. Arai, K. Ohira et al., "Chromatic Dispersion Free Fourier Transform-Based Wavelength Splitters for D-WDM," in Proc. *OECC*, paper 13B2-2, 2000.
[33] C. Dragone, "Frequency routing device having a wide and substantially flat passband," U.S. Patent 5488680, 1996.
[34] C. R. Doerr, M. A. Cappuzzo, E. Y. Chen et al., "Low-loss rectangular-passband multiplexer consisting of a waveguide grating router synchronized to a three-arm interferometer," *IEEE Photon. Technol. Lett.*, 17, 2334–2336, November 2005.
[35] C. R. Doerr, M. A. Cappuzzo, E. Y. Chen et al., "Wide-band arrayed waveguide grating with three low-loss maxima per passband," *IEEE Photon. Technol. Lett*., 18, 2308–2310, November 2006.
[36] P. A. Besse, M. Bachmann, C. Nadler, and H. Melchior, "The integrated prism interpretation of multileg Mach-Zehnder interferometers based on multimode interference couplers," *Opt. Quantum Electron.*, 27, 909–920, 1995.
[37] C. R. Doerr, M. Cappuzzo, E. Laskowski et al., "Dynamic wavelength equalizer in silica using the single-filtered-arm interferometer," *IEEE Photon. Technol. Lett.*, 11, 581–583, May 1999.
[38] C. Dragone, "An $N \times N$ optical multiplexer using a planar arrangement of two star couplers," *IEEE Photon. Technol. Lett.*, 3, 812–815, 1991.
[39] C. R. Doerr, "Beam propagation method tailored for step-index waveguides," *IEEE Photon. Technol. Lett.*, 13, 130–132, February 2001.
[40] Y. P. Li, "Optical device having low insertion loss," U.S. Patent No. 5745618, April 28, 1998.
[41] A. Sugita, A. Kaneko, K. Okamoto et al., "Very low insertion loss arrayed-waveguide grating with vertically tapered waveguides," *IEEE Photon. Technol. Lett.*, 12, 1180–1182, September 2000.
[42] K. Maru, T. Chiba, M. Okawa et al., "Low-loss arrayed-waveguide grating with high index regions at slab-to-array interface," *Electron. Lett.*, 37, 1287–1289, 2001.
[43] C. R. Doerr, R. Pafchek, and L. W. Stulz, "16-band integrated dynamic gain equalization filter with less than 2.8-dB insertion loss," *IEEE Photon. Technol. Lett.*, 14, 334–336, March 2002.
[44] C. R. Doerr, C. H. Joyner, and L. W. Stulz, "Integrated WDM dynamic power equalizer with potentially low insertion loss," *IEEE Photon. Technol. Lett.*, 10, 1443–1445, October 1998.
[45] C. R. Doerr, R. Pafchek, and L. W. Stulz, "Integrated band demultiplexer using waveguide grating routers," *IEEE Photon. Technol. Lett.*, 15, 1088–1090, August 2003.
[46] G. Lenz, B. J. Eggleton, C. K. Madsen et al., "Optical dispersion of optical filters for WDM systems," *IEEE Photon. Technol. Lett.*, 10, 567–569, April 1998.
[47] S. Chandrasekhar, C. R. Doerr, and L. L. Buhl, "Flexible waveband optical networking without guard bands using novel 8-skip-0 banding filters," *IEEE Photon. Technol. Lett.*, 17, 579–581, March 2005.
[48] C. R. Doerr, M. Cappuzzo, L. Gomez et al., "Planar ligthwave circuit eight-channel CWDM multiplexer with $<$3.9-dB insertion loss," *J. Lightw. Technol.*, 23, 62–65, January 2005.
[49] G. Heise, H. W. Schneider, and P. C. Clemens, "Optical Phased Array Filter Module with Passively Compensated Temperature Dependence," in Proc. *ECOC '98*, Madrid, Spain, September 20–24, 1998, pp. 319–320.
[50] Y. Inoue, A. Kaneko, F. Hanawa et al., "Athermal silica-based arrayed-waveguide grating multiplexer," *Electron. Lett.*, 33, 1945–1946, 1997.
[51] R. Gao, K. Takayama, A. Yeniay, and A. F. Garito, "Low-Insertion Loss Athermal AWG Multi/Demultiplexer Based on Perfluorinated Polymers," in Proc. *ECOC '02*, 6.2.2, Copenhagen, Denmark, September 8–12, 2002.
[52] J. B. D. Soole, M. Schlax, C. Narayanan, and R. Pafchek, "Athermalisation of silica arrayed waveguide grating multiplexers," *Electron. Lett.*, 39, 1182–1184, 2003.
[53] A. Kaneko, S. Kamei, Y. Inoue et al., "Athermal Silica-Based Arrayed-Waveguide Grating (AWG) Multiplexers with New Low Loss Groove Design," in Proc. *OFC-IOOC '99*, TuO1, San Diego, CA, 1999, pp. 204–206.
[54] K. Takada, M. Abe, T. Shibata, and K. Okamoto, "10 GHz-spaced 1010-channel Tandem AWG filter consisting of one primary and ten secondary AWGs," *IEEE Photon. Technol. Lett.*, 13, 577–578, 2001.

[55] K. Takada, M. Abe, T. Shibata, and K. Okamoto, "Three-stage ultra-high-density multi/demultiplexer covering low-loss fiber transmission window 1.26–1.63 μm," *Electron. Lett.*, 38, 405–406, 2002.

[56] K. Takada, M. Abe, T. Shibata, and K. Okamoto, "A 25-GHz-spaced 1080-channel tandem multi/demultiplexer covering the S-, C-, and L-bands using an arrayed-waveguide grating with Gaussian passbands as a primary filter," *IEEE Photon. Technol. Lett.*, 14, 648–650, 2002.

[57] K. Takada, M. Abe, T. Shibata, and K. Okamoto, "5 GHz-spaced 4200-channel two-stage tandem demultiplexer for ultra-multi-wavelength light source using supercontinuum generation," *Electron. Lett.*, 38, 572–573, 2005.

[58] C. R. Doerr, M. Shirasaki, and C. H. Joyner, "Chromatic focal plane displacement in the parabolic chirped waveguide grating router," *IEEE Photon. Technol. Lett.*, 9, 625–627, May 1997.

[59] C. R. Doerr and C. H. Joyner, "Double-chirping of the waveguide grating router," *IEEE Photon. Technol. Lett.*, 9, 776–778, June 1997.

[60] C. R. Doerr, L. W. Stulz, R. Pafchek et al., "Potentially low-cost widely tunable laser consisting of a semiconductor optical amplifier connected directly to a silica waveguide grating router," *IEEE Photon. Technol. Lett.*, 15, 1446–1448, October 2003.

[61] A. Rigny, A. Bruno, and H. Sik, "Multigrating method for flattened spectral response wavelength multi/demultiplexer," *Electron. Lett.*, 33, 1701–1702, 1997.

[62] C. R. Doerr, L. W. Stulz, J. Gates et al., "Arrayed waveguide lens wavelength add-drop in silica," *IEEE Photon. Technol. Lett.*, 11, 557–559, May 1999.

[63] D. Iazikov, C. M. Greiner, and T. W. Mossberg, "Integrated holographic filters for flat passband optical multiplexers," *Opt. Express*, 14, 3497–3502, 2006.

[64] K. Okamoto, M. Okuno, A. Himeno, and Y. Ohmori, "16-channel optical add/drop multiplexer consisting of arrayed-waveguide gratings and double-gate switches," *Electron. Lett.*, 32, 1471–1472, 1996.

[65] T. Saida, A. Kaneko, T. Goh et al., "Athermal silica-based optical add/drop multiplexer consisting of arrayed waveguide gratings and double gate thermo-optical switches," *Electron. Lett.*, 36, 528–529, 2000.

[66] A. Sugita, K. Jinguji, N. Takato et al., "Bridge-Suspended Thermo-Optic Phase Shifter and its Application to Silica-Waveguide Optical Switch," in Proc. *IOOC '89*, paper 18D1-4, 1989, p. 58.

[67] R. Kasahara, M. Yanagisawa, A. Sugita et al., "Low-power consumption silica-based 2×2 thermooptic switch using trenched silicon substrate," *IEEE Photon. Technol. Lett.*, 11, 1132–1134, 1999.

[68] C. R. Doerr, L. W. Stulz, M. Cappuzzo et al., "40-wavelength add-drop filter," *IEEE Photon. Technol. Lett.*, 11, 1437–1439, November 1999.

[69] C. R. Doerr, L. W. Stulz, R. Monnard et al., "40-wavelength planar channel-dropping filter with improved crosstalk," *IEEE Photon. Technol. Lett.*, 13, 1008–1010, September 2001.

[70] C. R. Doerr, L. W. Stulz, R. Pafchek, and S. Shunk, "Compact and low-loss manner of waveguide grating router passband flattening and demonstration in a 64-channel blocker/multiplexer," *IEEE Photon. Technol. Lett.*, 14, 56–58, January 2002.

[71] C. R. Doerr, L. W. Stulz, M. Cappuzzo et al., "2×2 wavelength-selective cross connect capable of switching 128 channels in sets of eight," *IEEE Photon. Technol. Lett.*, 14, 387–389, March 2002.

[72] C. R. Doerr, L. W. Stulz, D. S. Levy et al., "Eight-wavelength add-drop filter with true reconfigurability," *IEEE Photon. Technol. Lett.*, 15, 138–140, January 2003.

[73] C. R. Doerr, L. W. Stulz, D. S. Levy et al., "Wavelength add-drop node using silica waveguide integration," *J. Lightw. Technol.*, 22, 2755–2757, December 2004.

[74] A. M. Weiner, J. P. Heritage, and E. M. Kirshner, "High-resolution femtosecond pulse shaping," *J. Opt. Soc. Am. B.*, 5, 1563–1572, 1988.

[75] K. Okamoto, T. Kominato, H. Yamada, and T. Goh, "Fabrication of frequency spectrum synthesiser consisting of arrayed-waveguide grating pair and thermo-optic amplitude and phase controllers," *Electron. Lett.*, 35, 733–734, 1999.
[76] A. M. Weiner, J. P. Heritage, and R. N. Thurston, "Synthesis of phase coherent, picosecond optical square pulses," *Opt. Lett.*, 11, 153–155, 1986.
[77] S. Kawanishi, H. Takara, T. Morioka et al., "200 Gbit/s, 100 km time-division-multiplexed optical transmission using supercontinuum pulses with prescaled PLL timing extraction and all-optical demultiplexing," *Electron. Lett.*, 31, 816–817, 1995.
[78] K. Takiguchi, K. Okamoto, T. Kominato et al., "Flexible pulse waveform generation using a silica waveguide-based spectrum synthesis circuit," *Electron. Lett.*, 40, 537–538, 2004.
[79] C. R. Doerr, S. Chandrasekhar, P. J. Winzer et al., "Simple multichannel optical equalizer mitigating intersymbol interference for 40-Gb/s nonreturn-to-zero signals," *J. Lightw. Technol.*, 22, 249–251, January 2004.
[80] M. Bohn, G. Mohs, C. Scheerer et al., "An Adaptive Optical Equalizer Concept for Single Channel Distortion Compensation," in Proc. *ECOC*, Mo.F.2.3, 2001.
[81] A. H. Gnauck, G. Charlet, P. Tran et al., "25.6- Tb/s C+L-Band Transmission of Polarization-Multiplexed RZ-DQPSK Signals," in Proc. *OFC*, PDP19, 2007.
[82] C. R. Doerr, P. J. Winzer, G. Raybon et al., "A Single-Chip Optical Equalizer Enabling 107-Gb/s Optical Non-Return-to-Zero Signal Generation," in Proc. *ECOC*, post deadline paper, 2005.
[83] M. Bohn, W. Rosenkranz, P. M. Krummrich et al., "Experimental Verification of Combined Adaptive PMD and GVD Compensation in a 40 Gb/s Transmission Using Integrated Optical FIR-Filters and Spectrum Monitoring," in Proc. *OFC*, TuG3, 2004.
[84] D. M. Gill, M. S. Rasras, X. Liu et al., "CMOS Compatible Guided-Wave Tunable Optical Equalizer," in Proc. *OFC* Anaheim, OTuM6, 2007.
[85] C. K. Madsen and J. H. Zhao, *Optical Filter Design and Analysis*, John Wiley and Sons, 1999.
[86] F. Hosrt, C. Berendsen, R. Beyeler et al., "Tunable Ring Resonator Dispersion Compensators Realized in High-Refractive-Index Contrast SiON Technology," in Proc. *ECOC*, PD paper 2.2, 2000.
[87] W. Chen, S. Chu, B. Little et al., "Compact, Full C-Band, Widely Tunable Optical Dynamic Dispersion Compensators" in Proc. *OFC*, paper PDP8, 2006.
[88] B. J. Eggleton, A. Ahuja, P. S. Westbrook et al., "Integrated tunable fiber grating for dispersion management in high-bit rate systems," *J. Lightw. Technol.*, 18, 1418–1432, October 2000.
[89] Y. Hibino, T. Kitagawa, K. O. Hill et al., "Wavelength division multiplexer with photoinduced Bragg gratings fabricated in a planar-lightwave-circuit-type asymmetric Mach-Zehnder interferometer on Si," *IEEE Photon. Technol. Lett.*, 8, 84–86, January 1996.
[90] L. Eldada and L. W. Shacklette, "Advances in polymer integrated optics," *IEEE J. Sel. Top. Quantum Electron.*, 6, 54–68, 2000.
[91] K. Takiguchi, K. Jinguji, K. Okamoto, and Y. Ohmori, "Variable group-delay dispersion equalizer using lattice-form programmable optical filter on planar lightwave circuit," *IEEE J. Sel. Top. Quantum Electron.*, 2(2), 270–276, June 1996.
[92] H. Kawashima, N. Matsubara, and K. Nara, "Tunable dispersion compensator using PLC type optical transversal filter," Furukawa Review, no. 29, 13–18, 2006.
[93] C. R. Doerr, L. Zhang, L. L. Buhl et al., "40-Gb/s Modulator With Monolithically Integrated Tunable Dispersion Compensator," in Proc. *OFC*, PDP45, 2007.
[94] C. R. Doerr, S. Chandrasekhar, L. L. Buhl et al., "Optical dispersion compensator suitable for use with non-wavelength-locked transmitters," *J. Lightw. Technol.*, 24, 166–170, January 2006.
[95] C. R. Doerr, S. Chandrasekhar, M. A. Cappuzzo et al., "Four-stage Mach-Zehnder-type tunable optical dispersion compensator with single-knob control," *IEEE Photon. Technol. Lett.*, 17, 2637–2639, December 2005.
[96] Y. Yamauchi, H. Sonoda, H. Furukawa, and Y. Kubota, "Variable Dispersion Compensation Using a VIPA With an Extended Bandwidth," in Proc. *ECOC*, paper Th 1.5.3, 2005.

[97] D. T. Neilson, R. Ryf, F. Pardo, V. A. Aksyuk, M.-E. Simon, D. O. Lopez, D. M. Marom, S. Chandrasekhar, "MEMS-based channelized dispersion compensator with flat passbands," *J. Lightw. Technol.*, 22, 101–105, January 2004.

[98] C. R. Doerr, L. W. Stulz, S. Chandrasekhar, and R. Pafchek, "Colorless tunable dispersion compensator with 400-ps/nm range integrated with a tunable noise filter," *IEEE Photon. Technol. Lett.*, 15, 1258–1260, September 2003.

[99] D. M. Marom, C. R. Doerr, M. A. Cappuzzo et al., "Compact colorless tunable dispersion compensator with 1000-ps/nm tuning range for 40-Gb/s data rates," *J. Lightw. Technol.*, 24, 237–241, January 2006.

[100] C. R. Doerr, R. Blum, L. L. Buhl et al., "Colorless tunable optical dispersion compensator based on a silica arrayed-waveguide grating and a polymer thermooptic lens," *IEEE Photon. Technol. Lett.*, 18, 1222–1224, June 2006.

[101] Y. Painchaud, A. Maillux, H. Chotard et al., "Multi-Channel Fiber Bragg Gratings for Dispersion and Slope Compensation," in Proc. *OFC*, ThAA5, 2002.

[102] G. Shabtay, D. Mendlovic, and Y. Itzhar, "Optical Single Channel Dispersion Compensation Devices and Their Application," in Proc. *ECOC*, We1.2.1, 2005.

[103] L. Gruner-Nielsen, M. Wandel, P. Kristensen et al., "Dispersion-compensating fibers," *J. Lightw. Technol.*, 23, 3566–3579, November 2005.

[104] R. Nagarajan et al., "Large-scale photonic integrated circuits," *IEEE J. Sel. Top. Quantum Electron.*, 11, 50–65, 2005.